Deep–Sea Research II 221 (2025) 105464

Contents lists available at ScienceDirect

Deep-Sea Research Part II

journal homepage: www.elsevier.com/locate/dsr2

Variability of bottom dissolved oxygen on the southern Senegalese shelf at intraseasonal to interannual time scales using a modelling approach

Abdoul Wahab Tall [a,b,*], Vincent Echevin [c], Xavier Capet [c], Eric Machu [d]

[a] Department of Earth, Ocean and Atmospheric Sciences, University of British Columbia, 2020 – 2207 Main Mall, Vancouver, V6T 1Z4, British Columbia, Canada
[b] Laboratoire de Physique de l'Atmosphère et de l'Océan Siméon Fongang, Université Cheikh Anta DIOP de Dakar, Ecole Supérieure Polytechnique, Dakar-Fann, 5085, Senegal
[c] LOCEAN-IPSL, IRD/CNRS/Sorbonne Université (UPMC)/MNHN, UMR 7159, 4, place Jussieu, Paris, 75005, France
[d] Université de Bretagne Occidentale, CNRS, IRD, Ifremer, Laboratoire d'Océanographie Physique et Spatiale (LOPS), IUEM, UMR 6523, Brest, 29280, France

ARTICLE INFO

Keywords:
Dissolved oxygen
Modelling
Senegalese shelf
CROCO-PISCES

ABSTRACT

Recent in-situ measurements on the west African continental shelf have shown that the bottom waters undergo episodic hypoxia and even anoxia. In this study, we investigate the variability of bottom dissolved oxygen (DO) over the southern Senegalese shelf at seasonal, intraseasonal and interannual time scales over the period 2015–2019 using a high-resolution (2 km) regional coupled dynamical-biogeochemical model. The model is forced by daily winds to represent synoptic variability during the upwelling-favourable cold season (November-May). Near-bottom DO evaluation using data from the Melax mooring located over the mid shelf indicates that the model represents well the seasonal and intraseasonal variability. A bottom DO budget shows that advection of deep, low-oxygenated waters over the shelf edge during the upwelling season generates a DO loss, which is overcompensated by ventilation of the entire shelf due to vertical mixing. Biogeochemical processes compensate this DO supply: DO is consumed by organic matter and zooplankton respiration, slightly compensated by regenerated and new primary production. Because of a sluggish shelf circulation during the summer season (July–September, JAS), oxygen concentration declines in parts of the outer shelf bottom layer, in spite of a weaker surface primary production and organic matter export than during the heart of the cold season (February–April, FMA). Analysis of the synoptic variability reveals the complexity of the DO response to the duration and intensity of upwelling and relaxation events, with the largest DO decrease of $\sim 110 \mu mol O_2 L^{-1}$ associated with a strong upwelling event (cumulative upwelling index $\sim 2 Nm^{-2} day$) obtained in 2016. Year to year variability indicates two periods of enhanced hypoxia in FMA 2017 and JAS 2016 characterized by a high retention of bottom waters over the shelf.

1. Introduction

The ocean is losing its breath, at global scale and in many coastal regions. Observation-based studies found a deoxygenation trend over the past decades in the global ocean (Schmidtko et al., 2017) resulting in a reduction of global-mean dissolved oxygen (DO) concentration of 2% since 1960, while earth system models project a DO decline of 1%–7% by 2100 (Keeling et al., 2010; Long et al., 2016; Kwiatkowski et al., 2020). This deoxygenation trend has been attributed to a reduced ventilation of deep waters due to increased stratification, combined with thermally driven decreased oxygen solubility (Bopp et al., 2013; Oschlies et al., 2018).

Global warming exacerbates oxygen depletion in nutrient-enriched coastal regions (Rabalais et al., 2014; Altieri et al., 2015; Breitburg et al., 2018), where deoxygenation due to anthropogenic land-use change and nutrient loading is generally larger than offshore (Gilbert et al., 2010; Bograd et al., 2019). The combined effects of (i) higher nutrient concentrations (enhancing primary production), particulate organic matter (POM) export and DO consumption through organic matter (OM) remineralization at depth, and (ii) decreased ventilation due to a stronger stratification of surface waters, play an important role on increasing or decreasing oxygen levels. Very low DO concentrations ($\sim$6 $\mu molO_2L^{-1}$) lead to extensive "dead zones", as off Ivory Coast and Ghana in the Tropical North Eastern Atlantic Ocean (Altieri and Gedan, 2015). The frequency of these anoxic events and their associated disastrous effects is increasing (Grantham et al., 2004; Chan et al., 2008), generating more interest in the field of monitoring DO systems (Pitcher

* Corresponding author at: Department of Earth, Ocean and Atmospheric Sciences, University of British Columbia, 2020 – 2207 Main Mall, Vancouver, V6T 1Z4, British Columbia, Canada.
E-mail address: atall@eoas.ubc.ca (A.W. Tall).

https://doi.org/10.1016/j.dsr2.2025.105464

Available online 27 February 2025

et al., 2021).

In the Southern Senegal Upwelling Sector (SSUS) located within the West African Eastern Boundary Upwelling System (EBUS), surface winds drive the coastal upwelling of cold, nutrient-rich subsurface waters over the Senegalese continental shelf during the boreal winter–spring season (Roy, 1989; Ndoye et al., 2014). The west African coastal ocean is bordered by an oxygen minimum zone (OMZ) composed of a shallow (~100 m) and deep (~400 m) DO minimum (Brandt et al., 2015; Thomsen et al., 2019). While waters from the deep OMZ hardly reach the surface (Glessmer et al., 2009), the Senegalese shelf is directly connected to the relatively shallow OMZ, which supplies low DO waters to the shelf during the upwelling season (Tall et al., 2021; Capet et al., 2017). On the other hand, the west African boundary current (WABC; Barton, 1998; Kounta et al., 2018) flowing northward over the west African shelf and slope transports relatively DO-rich waters over the SSUS shelf during upwelling relaxation periods (Tall et al., 2021). Recent observations suggest that the SSUS shelf has already suffered episodes of anoxia: a short-lived (2 day-long) anoxic event (associated with nitrogen loss through denitrification) was uncovered in March 2012 (Machu et al., 2019), likely a consequence of diatom degradation during a prolonged wind relaxation.

The heavily exploited SSUS pelagic resources are also sensitive to DO variations. Low DO events (DO<10 $\mu molO_2L^{-1}$) contribute to changes in the abundance, distribution and migration pathways of several exploited marine species (Cheung et al., 2013); *e.g. Epinephelus aeneus* ("thiof") in the SSUS (Rose et al., 2019). To the best of our knowledge, there is only a single report of high fish mortality event that may be attributed to deoxygenation (*i.e. Serranidae*, Caverivière and Touré, 1990) but this may be a consequence of limited monitoring. The extent and frequency of hypoxic events remain unknown due to the lack of observations on the Senegalese shelf. Furthermore, the physical and/or biogeochemical conditions triggering these events are poorly understood.

Biogeochemical modelling has proven to be essential to understand the processes driving DO variability. Several regional model studies have focused on the DO content of upwelling source waters and their implications on oxygen depletion in different EBUS (*e.g.* (Espinoza-Morriberón et al., 2019, 2021) for the Peru EBUS; Schmidt and Eggert (2016) for the Benguela EBUS; Siedlecki et al. (2015) for the Washington shelf). The latter suggested that half of the seasonal oxygen decline over the shelf was due to advection of low-DO waters and half to local respiration. Using a Nutrient–Phytoplankton–Zooplankton–Detritus (NPZD)-like regional model, Koch et al. (2017) found that the mechanism most responsible for Oregon shelf hypoxia was coastal upwelling, although partly compensated by DO production by biological processes. While the production and transport mechanisms of planktonic biomass in the west african EBUS have been investigated using a regional model (Auger et al., 2016), the DO dynamics over the south Senegalese shelf at seasonal and interannual time scales remains unexplored using biogeochemical modelling. In the following we aim to (i) describe and evaluate the coupled physical-biogeochemical model and (ii) unravel the key aspects of near-bottom DO dynamics over the SSUS continental shelf: vertical distribution, sector-scale spatial patterns, temporal fluctuations on synoptic to interannual time scales and identification of the underlying processes.

2. Model description and configuration

2.1. The CROCO hydrodynamical model

The Coastal and Regional Ocean Community (CROCO; Hilt et al., 2020) hydrodynamic model is used to simulate ocean dynamics in the SSUS. The so-called *can11* configuration at 10 km resolution has 50 terrain-following sigma levels in the vertical and covers west Africa [7° N-35° N; 30° W-10° W] (Ndoye et al., 2017). This "parent" grid is coupled using AGRIF (Adaptive Grid Refinement in Fortran; Debreu et al., 2012) to the *sen2* "child" grid at 2 km resolution within the area [12° N-18° N; 20° W-15° W] which encompasses the entire Senegalese shelf (Fig. 1a, Ndoye, 2016; Ndoye et al., 2017). The topography used in both grids is the high resolution 30" version of GEBCO (General Bathymetric Chart of the Oceans), locally modified using bathymetric charts (see Ndoye et al., 2017 for details). Bottom topography is then smoothed to reduce errors associated with the calculation of the horizontal pressure gradient when sigma coordinates are utilized (Beckmann and Haidvogel, 1993). Horizontal advection of biogeochemical tracers (*e.g.* DO) is performed using the quasi-monotone WENO5 (Weighted Essentially Non-oscillatory fifth-Order) scheme to avoid the generation of negative values. Vertical mixing is performed using the K-Profile parameterization (Large et al., 1994). More details on the model setup can be found in Ndoye (2016).

2.2. The biogeochemical PISCES model

The Pelagic Interaction Scheme for Carbon and Ecosystem Studies (PISCES) biogeochemical model (Aumont and Bopp, 2006; Aumont et al., 2015) is coupled to CROCO to study biophysical processes in the SSUS. PISCES simulates the biogeochemical cycles of carbon, nitrogen, phosphorus, silicate, iron and DO. The model includes five limiting nutrients (ammonium, nitrate, phosphate, silicate, and iron), two phytoplankton compartments (nanophytoplankton and diatoms), two zooplankton size classes (micro- and mesozooplankton) and three non-living organic matter (OM) compartments (Dissolved Organic Matter, small and big Particulate Organic Matter (POM)). Variables such as carbon, nitrogen and oxygen are related by assumed constant Redfield ratios (Redfield et al., 1963; Takahashi et al., 1985; Körtzinger et al., 2001). The detailed description of the model can be found in Aumont et al. (2015). In the model version used in this study, there is no decomposition of OM in the sediment nor nutrient and DO fluxes at the sediment-sea water interface.

2.3. Model forcing

An interannual simulation covering the period March 2014–December 2019 is performed. For atmospheric forcing, we use the Advanced Scatterometer (ASCAT) daily wind stress gridded product processed by Satellite Data Processing and Distribution Center (CERSAT, Bentamy and Fillon (2012); downloaded from https://cersat.ifremer.fr/); climatological heat and freshwater fluxes from Comprehensive Ocean-Atmosphere Dataset (COADS, Worley et al., 2005); restoring to a climatological Sea Surface Temperature (SST) product (Ndoye et al., 2014) using (Barnier et al., 1995)'s parameterization. River runoff (from the Senegal, Gambia and Casamance rivers) is not explicitly taken into account, but represented via a restoring of the model Sea Surface Salinity (SSS) to COADS climatological SSS.

The MERCATOR model (GLOBAL-ANALYSISFORECAST-PHY-001-024; 1/12° resolution; downloaded from http://marine.copernicus.eu/) daily outputs are used to force time-varying physical properties (temperature, salinity, velocity and sea level) at *can11* open boundary conditions (OBC).

Climatological data from the World Ocean Atlas (WOA) (Garcia et al., 2019) and Global Ocean Data Analysis Project (GLODAP, Key et al., 2004) are used for nutrients/oxygen and dissolved inorganic/organic carbon monthly climatological OBC, respectively. A climatological atmospheric dust deposit (iron) is also used (Tegen and Fung, 1994).

The ocean state on March 1st year 10 of a climatological CROCO-PISCES simulation is used as initial condition. This climatological simulation was forced by monthly climatological wind stress (Scatterometer Climatology of Ocean Winds (SCOW), Risien and Chelton, 2008) and by climatological buoyancy forcing (as previously described). Climatological OBC were provided by the Mercator Global Ocean Reanalysis (GLORYS; 1/4° resolution; Ferry et al., 2010) for the physics and by the previously described climatologies for biogeochemistry.

The CROCO-PISCES standard variables, biogeochemical flux terms and oxygen budget terms (see Section 2.4) are saved at a daily frequency.

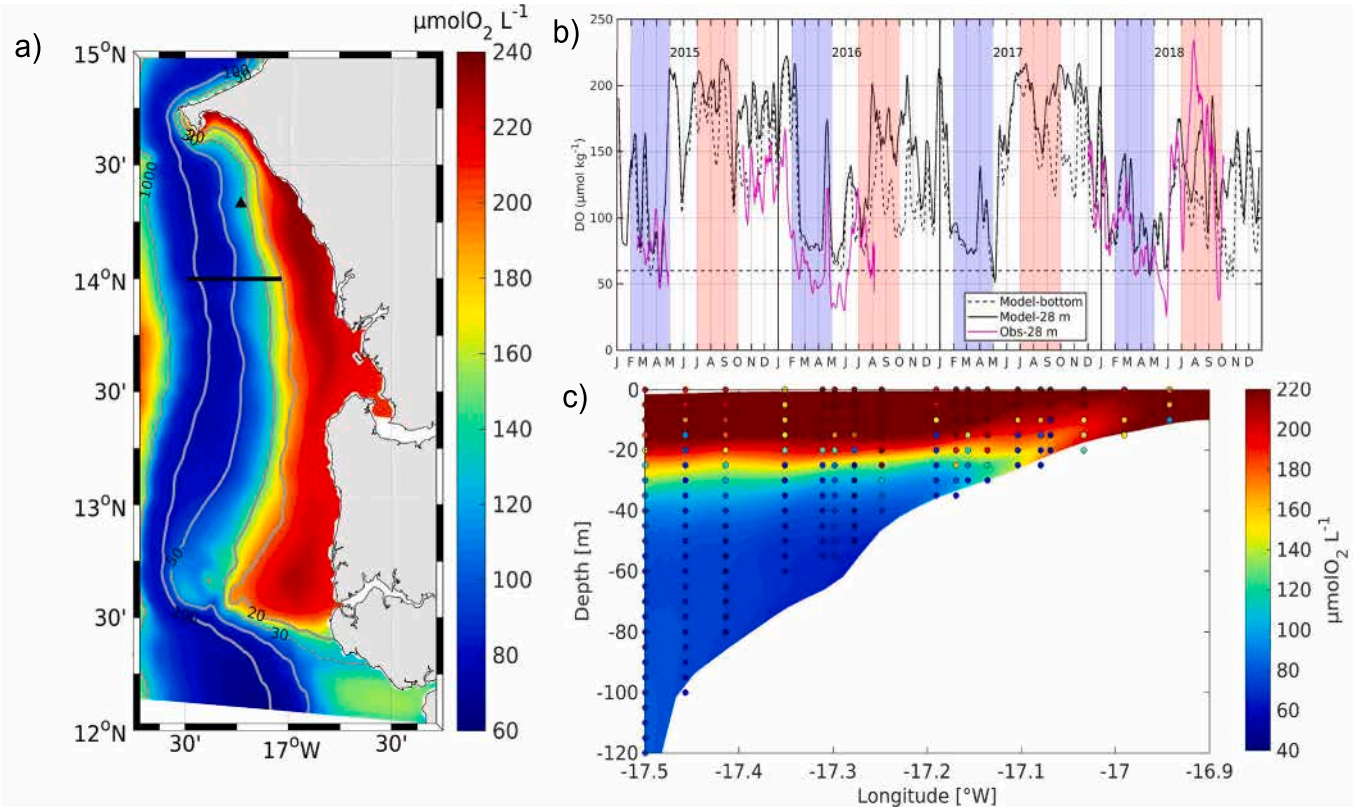

Fig. 1. (a) Annual-mean (2015–2019 average) modelled bottom dissolved oxygen (DO) over the south Senegalese shelf and slope. 20, 30, 50, 100, 1000 m isobaths are indicated by grey lines. Note that the 2 km model grid is larger than the region shown in (a) ; (b) DO at 28 m depth: model (black full line) and Melax observations (cyan line; Melax mooring location is indicated by a black triangle in (a)). The dashed line marks the modelled bottom DO (35 m depth). Blue (resp. pink) shading indicate the core of the upwelling season (February–March–April) (resp. the warm season (July–August–September)); (c) DO cross-shelf section at 14° N (see black line in (a)) from UPSEN2-ECOAO cruise (February 21–March 18, 2013, coloured circles) and model (DO composite obtained by averaging FMA 2015 daily sections under similar wind conditions as in February 21-March 18, 2018).

2.4. Oxygen dynamics

Modelled DO is represented by the following equation:

$$\frac{\partial O_2}{\partial t} = \overbrace{(\frac{\partial O_2}{\partial t})_{Bio}}^{\text{biological sources and sinks}} + \overbrace{(\frac{\partial O_2}{\partial t})_{Dyn}}^{\text{dynamical transport}} + \overbrace{O_{2flux}}^{\text{flux air-sea}} \quad (1)$$

where $(\partial_t O_2)_{Bio}$ represents biogeochemical oxygen sources and sinks, $(\partial_t O_2)_{Dyn}$ represents dynamic oxygen transport processes, O_{2flux} represents the oxygen flux at the air-sea interface. The biogeochemical term is calculated as follows:

$$\begin{aligned}(\frac{\partial O_2}{\partial t})_{Bio} = {} & \overbrace{O_2^{ut}(\mu^P_{NH_4}P + \mu^D_{NH_4}D)}^{\text{Prod. by regenerated production}} + \overbrace{(O_2^{ut}+O_2^{nit})(\mu^P_{NO_3}P + \mu^D_{NO_3}D)}^{\text{Prod. by new production}} \\ & + \overbrace{O_2^{nit}N_{fix}}^{\text{Prod. by nitrogen fixation}} - \overbrace{O_2^{ut}\gamma^Z(1-e^Z-\sigma^Z)\sum_i g^Z(l)Z}^{\text{Respiration by microzooplankton}} \\ & - \overbrace{O_2^{ut}\gamma^M(1-e^M-\sigma^M)(\sum_i g^M(I)+\sum_i g^M_{FF}(I))M - O_2^{ut}\gamma^M R^M_{up}}^{\text{Respiration by mesozooplankton}} \\ & - \overbrace{O_2^{nit}NITRIF}^{\text{Consumption by nitrification}} - \overbrace{O_2^{ut}REMIN}^{\text{Consumption by remineralization}}\end{aligned} \quad (2)$$

OM and DO are produced by primary production, *i.e.* the assimilation of nutrients by nanophytoplankton (P) and diatoms (D) during photosynthesis (first and second terms of Eq. (2)). Primary production consists in (i) regenerated production based on the ammonium consumption and (ii) new production based on nitrate consumption. All the production/consumption terms initially in carbon units are multiplied by stoichiometric O/C Redfield ratios for O_2^{ut} and O_2^{nit} for conversion into oxygen units. Their values have been set to 140:122 and 32:122, respectively (Takahashi et al., 1985). O_2^{ut} accounts for the change in oxygen relative to carbon during ammonium conversion into OM. Thus it is the stoichiometric ratio used when phytoplankton is taking up ammonium. When nitrate is used, it has to be reduced first to ammonium (using Nitrate Reductase and Nitrite Reductase) which implies the production of O_2^{nit} moles of oxygen. As a consequence, $(O_2^{nit} + O_2^{ut})$ moles of oxygen are produced when phytoplankton is growing using nitrate.

DO can also be produced by atmospheric nitrogen fixation (third term in Eq. (2)). In this parameterization, only the net effect of nitrogen fixation is represented ($N_2 -> OM -> NH_4$), thus $(O_2^{nit} + O_2^{ut})$ moles of oxygen are produced during the first reaction and O_2^{ut} moles of oxygen are removed during the second reaction. However, this source is negligible in our study area.

On the other hand, DO is consumed by respiration (hereafter $RESPZ$) of micro-(Z) and mesozooplankton (M) proportional to grazing pressure (*i.e.* the $g(I)Z$ terms in Eq. (2), with I the micro- and mesozooplankton preys), by remineralization of OM ($REMIN$), and by nitrification ($NITRIF$). The reader is referred to Aumont et al. (2015) for a detailed description of the model equations.

Physical terms, which can be sources or sinks of oxygen, are computed as follows:

$$(\frac{\partial O_2}{\partial t})_{Dyn} = \overbrace{-u_H\nabla_H O_2}^{\text{horizontal advection}} \overbrace{-w\nabla_z O_2}^{\text{vertical advection}} + \overbrace{\partial_z(K_z\partial_z O_2)}^{\text{vertical mixing}} \quad (3)$$

In the present study, we are mainly interested in the analysis of the bottom oxygen balance (see Section 5). The bottom boundary

condition (*i.e.* no flux through the bottom) ties the horizontal and vertical components of velocity in such a way that analysing separately horizontal and vertical advection is not meaningful, thus the sum of the two terms (*i.e.* total advection) is used in the following sections. The last term of Eq. (3) is vertical mixing, which tends to reduce DO vertical gradients. It depends on the vertical structures (first and second derivatives) of DO and of the vertical mixing coefficient (K_z) derived using KPP. Because of the implicit diffusion of the WENO5 advection scheme, no explicit horizontal mixing (*e.g.* using a Laplacian) is required. Thus the weak horizontal mixing of DO is lumped with the DO horizontal advection term.

Last, the DO flux at the air-sea interface (last term of Eq. (1)) resulting from the air-sea partial pressure difference, and from wind-induced turbulence is computed as follows:

$$O_{2flux} = k_w(\alpha.O_2^{atm} - O_2^{surf}) \tag{4}$$

with k_w the wind-dependant transfer velocity, α the temperature-dependant solubility of oxygen in seawater. The term in parenthesis is the difference in O_2 partial pressure between the atmosphere and the ocean surface layer. Note that the oxygen concentration in the atmosphere (O_2^{atm}) is assumed to be constant.

The air-sea flux enters the DO equation as a surface boundary condition for the vertical mixing term ($[K_z\partial_z O_2]_{z=0} = O_{2flux}$), so that vertical mixing conveys dissolved oxygen from the surface layer to the bottom layer. As bottom oxygen variability is the focus of our study, the air-sea fluxes (shown in Fig. S13) were not investigated.

2.5. Double time-integrals of DO budget terms and time-averaged DO anomalies

DO budgets terms, averaged over time periods of interest, are routinely used to interpret DO variations. However, analysing the impact of certain mechanisms (*e.g.* advection vs mixing, ...) on, say, DO averaged over a period of several months, is hindered when time-averaged values of the budget terms are used. To illustrate this caveat, we take the DO budget equation written in the simplified form:

$$\partial_t O_2 = R(t) \tag{5}$$

with $R(t)$ the sum of all the right hand-side in Eq. (1). Integrating Eq. (5) between an initial time t_0 and an arbitrary time t we obtain:

$$O_2(t) = O_2(t_0) + \int_{t_0}^{t} R(t)dt' \tag{6}$$

Averaging $O_2(t)$ between t_0 (*e.g.* February, 1st) and t_1(*e.g.* April, 30^{th}) (with $T = t_1 - t_0$) we obtain:

$$\frac{1}{T}\int_{t_0}^{t_1} O_2(t)dt = O_2(t_0) + \frac{1}{T}\int_{t_0}^{t_1}\int_{t_0}^{t} R(t)dt'dt \tag{7}$$

Consequently, the February–March–April (FMA) DO average is equal to the sum of the DO value on February first and of the double time-integral of each dynamical terms included in R (*e.g.* advection, vertical mixing, ...).

As daily-average dynamical terms ($< R(t) >$) are stored during the course of the simulation, we can approximate the double-time integral by:

$$\frac{1}{T}\int_{t_0}^{t_1}\int_{t_0}^{t} R(t)dt'dt = \frac{1}{T}\sum_{t_0}^{t_1}\sum_{t_0}^{t} < R(t) > +\epsilon \tag{8}$$

with ϵ a residual. This computation will be used to interpret inter-annual variations of FMA and JAS (July–August–September) DO (see Section 7.2) and discussed in Section 9.5.

2.6. Lagrangian analysis

To investigate the pathways and characteristics of SSUS shelf bottom waters, Lagrangian experiments using the Regional Ocean Modeling System Offline software (ROFF; Carr et al. (2008)) are carried out. Virtual floats representing water parcels are released in the bottom boundary layer (between the sea floor and ~10 meters above the sea floor) over sectors of the shelf (between 30 and 50 m depth). The floats are then transported by the currents backwards in time during 30 days. During their transit, DO concentrations and positions (latitude, longitude and depth) of the parcels are recorded every hour. This analysis is repeated each year (2015–2019), every 5 days between February 1st and April 30th and between July 1st and September 30th.

3. Observations

3.1. In situ observations

Bottom DO, temperature profiles and acoustic Doppler current profiler (ADCP) velocity measurements collected at the Melax mooring located over the SSUS shelf (14° 20.8'N-17° 13.68'W, Tall et al., 2021; Chabert et al., 2023) are used to evaluate the simulation. Each variable is available over a specific time period (including several gaps) between 2015 and 2018. More information on the mooring data (type of sensor, depth and time period for each variable) can be found in Tall et al. (2021). Data from cross-shore sections are also used, collected during (i) the UPSEN2-ECOAO campaign (DO; February–March 2013; 14° N; 0-120 m depth; Capet et al., 2017; Machu et al., 2019) and during (ii) two Amouage sailboat cruises (DO and temperature; June 13th, 2018 and November 19th, 2019; 13° 50′N; 0-100 m depth; E. Machu and X. Capet, personal communication). Nitrate from the Word Ocean Database (WOD, https://www.ncei.noaa.gov/products/world-ocean-atlas) are used to evaluate the modelled nitrate structure.

3.2. Satellite observations

CERSAT provided a daily Level 3 (L3) SST product with a resolution of 10 km as of January 2016. Surface chlorophyll (Chl-a) from the Self-Organizing Map and Neuro-Variational approach (SOM-NVA) was used (Correa et al., 2023). The absorbing properties of the Saharian aerosols transported over the ocean off west Africa are poorly accounted for in the standard ocean colour data processing algorithms. The SOM-NVA algorithm allows for a better representation of the optical thickness, a correction of the marine reflectance spectrum, and an increase in the spatio-temporal coverage of the area. The Chl-a estimates should thus be improved. Here, monthly SOM-NVA Chl-a data over 2015–2018 with a spatial resolution of 4 km are used. For comparison, the ESA-CCI (European Space Agency-Climate Change Initiative, Sathyendranath et al. (2019), https://data.marine.copernicus.eu/) surface Chl-a global product at 4 km resolution are also used.

4. Evaluation of modelled dissolved oxygen

A physical simulation using the same model settings and forced with a slightly different forcing was previously evaluated against satellite and in situ observations in Ndoye et al. (2017). For the sake of brevity, the comparison of modelled physical variables (temperature, mixed layer depth and velocity) and biogeochemical variables (surface chlorophyll and nitrate) with observations and associated figures are presented in the supplementary material.

The modelled and observed near-bottom DO time series are compared over the period 2015–2018 at the mooring location, located within a region of strong DO cross-shore gradient (Fig. 1a). A well-marked seasonal variability is found, with the lowest concentrations in the core of the upwelling season (FMA) and occasionally in May-June (Fig. 1b). The model DO is quite realistic during the 2015 cold

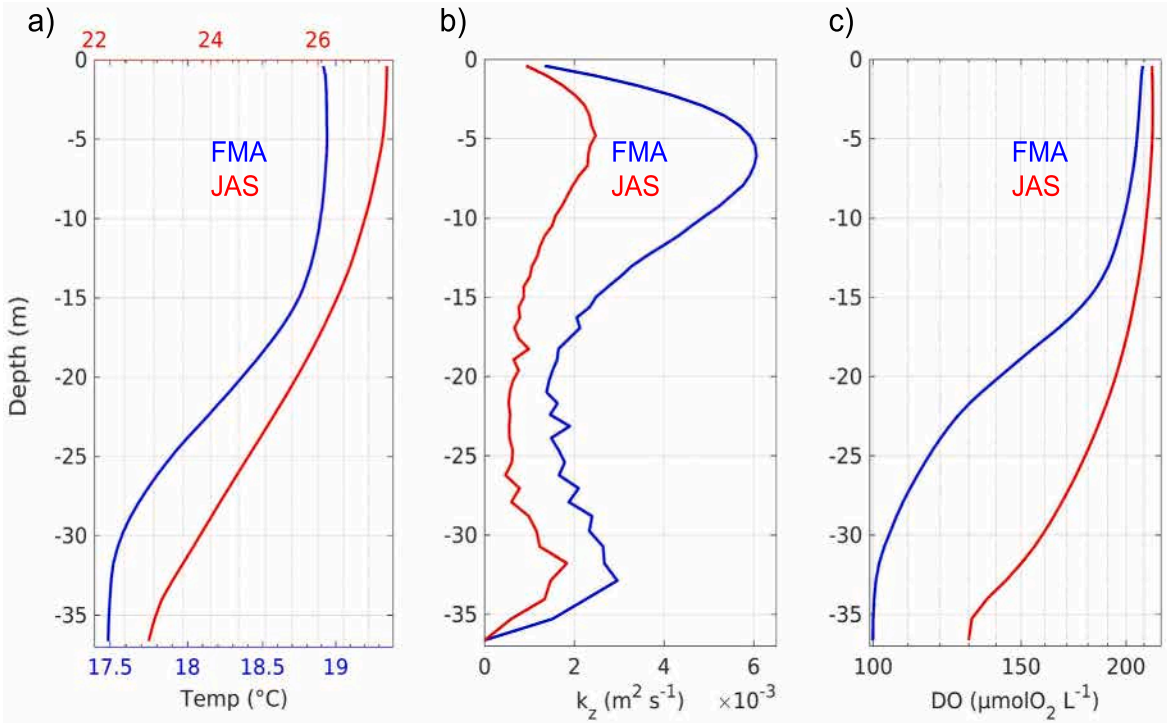

Fig. 2. Modelled profiles of (a) temperature, (b) vertical mixing coefficient (K_z) and (c) DO in FMA (blue) and JAS (red) averaged from 2015–2019 at Melax mooring location. Note the different temperature scales for FMA and JAS in (a).

season but too high during the 2016 cold season (leading to a model bias of ~20-25 µmol$O_2$$L^{-1}$). Model-data discrepancies are relatively low during the 2017–2018 cold season (December 2017–February 2018) but subsequently increase in late May 2018 as the model overestimates DO by ~20-25 µmol$O_2$$L^{-1}$.

Unfortunately, few observations are available during the warm season except in 2018, during which larger oscillations (between ~80 to 230 µmol$O_2$$L^{-1}$) are observed in situ than found in the model (between ~100 to 170 µmol$O_2$$L^{-1}$). Over the measured period, model DO levels lower than observed are only found over a short period in August 2018 with a ~50 µmol$O_2$$L^{-1}$ bias. We hypothesize that downwelling conditions led to the formation of a thick well oxygenated surface mixed layer which was not adequately reproduced by the model but lack data to confirm this (the thermistor chain and ADCP were not functioning at that time). Overall, intraseasonal variability driven by upwelling wind intensification and relaxation events and associated with meridional flow reversal over the SSUS shelf is relatively well reproduced, with peaks of DO frequently in phase between model and observations (*e.g.* in March–April 2015; Mid-April 2016; July 2015; February–March 2018; not shown; see Fig. 2 in Tall et al., 2021).

The model is also able to represent the cross-shore DO structure at 14° N (Fig. 1c). Note that the dates of the observed section (February–March 2013) are not included in the simulation period (2015–2019). Therefore, a situation from the model simulation in February–March 2015 with wind conditions close to those during the cruise (*i.e.* southwestward winds of ~3-8 ms^{-1}) is selected to provide a qualitative comparison. For both the model and observations, well-oxygenated surface waters (DO> 200 µmol$O_2$$L^{-1}$) are separated from less oxygenated subsurface waters (<100 µmol$O_2$$L^{-1}$) by a marked oxycline (located near ~25 m depth in the model). Low concentrations (down to ~50 µmol$O_2$$L^{-1}$) are observed over the slope (90-100 m) and over the mid-shelf (30-40 m depth). In contrast, modelled DO does not fall below ~100 µmol$O_2$$L^{-1}$ over the mid-shelf. A similar bias can also be seen in the November 2019 section (Figs. S2b,e). However, modelled DO is lower than 70 µmol$O_2$$L^{-1}$ over the mid-shelf (20 m depth) at other dates (*e.g.* March 1st, 2015; not shown). Overall, it remains difficult to estimate accurately the model DO bias given the scarcity of in situ data.

5. Dissolved oxygen and related mechanisms at the mid-shelf mooring site

5.1. DO seasonal variability and vertical structure

In this section, we examine the seasonal variation of the vertical structure of DO, temperature and vertical mixing coefficient over the northern SSUS mid-shelf at the mooring location (Fig. 2). The water column is less stratified during FMA (*i.e.* with a surface-bottom temperature difference of 1.5° *C*) than in JAS (surface-bottom temperature difference of ~4° *C*; Fig. 2a). Thermal stratification is enhanced (~0.1 ° Cm^{-1}) near 15-25 m depth in FMA whereas it is higher and nearly constant (~0.15 ° Cm^{-1}) over the whole water column in JAS.

The vertical mixing coefficient has two local maxima in the vertical (Fig. 2b): one in the surface mixed layer (SML; between 0-15 m depth) with a maximum at ~5 m depth and one in the bottom boundary layer (BBL) near ~32 m depth (*i.e.* 3-4 m above the bottom). The SML maximum is stronger in FMA (~ 6.10^{-3} m^2s^{-1}) than in JAS (~ 2.10^{-3} m^2s^{-1}) because of the stronger wind-driven mixing during the cold upwelling season. The BBL maximum is a consequence of the bottom friction. It is stronger in FMA (~ 3.10^{-3} m^2s^{-1}) than in JAS (~ 2.10^{-3} m^2s^{-1}) due to the FMA intensified wind-driven circulation (see below).

While SML waters are equally ventilated during both seasons (~200 µmol$O_2$$L^{-1}$; Fig. 2c), DO decreases rapidly with depth in FMA, forming a marked oxycline (~10 µmol$O_2$$L^{-1}$$m^{-1}$) near ~15-20 m depth and reaching 100 µmol$O_2$$L^{-1}$ in the bottom layer. In contrast, and despite less intense near-surface mixing, DO decrease with depth was weaker in JAS than in FMA, and bottom DO was larger (130 µmol$O_2$$L^{-1}$). Near the ocean floor, DO is homogeneous over a ~5 m-thick BBL in FMA whereas a marked oxycline is found above a thinner ~1-2 m-thick BBL in JAS (note that the use of 50 sigma levels in the vertical allows an adequate representation of even the thin summer BBL).

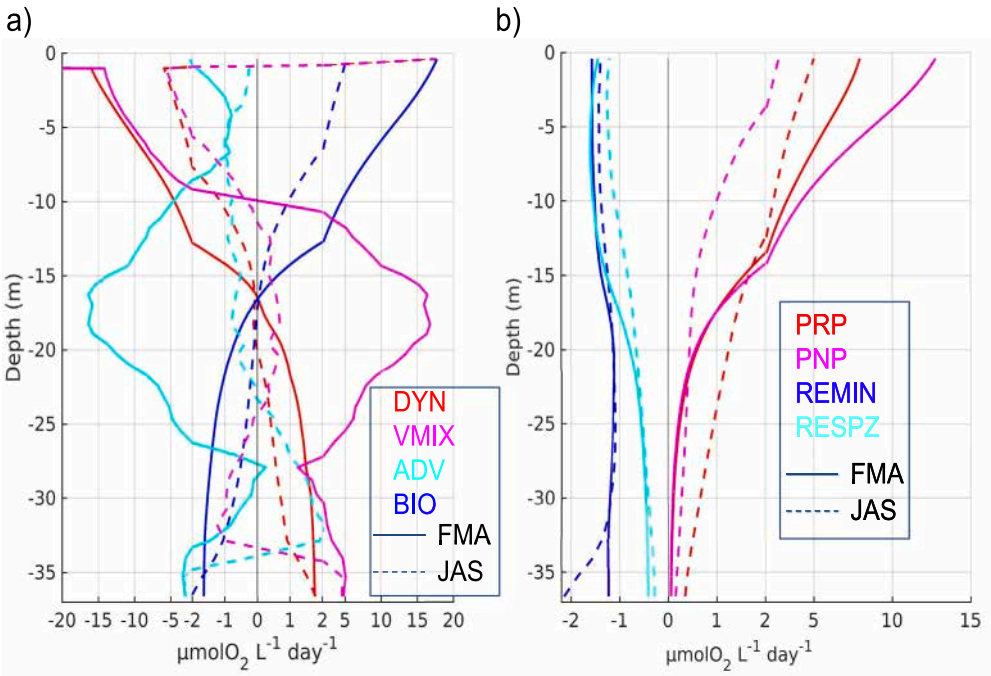

Fig. 3. Modelled vertical profiles of DO rates (in $\mu molO_2L^{-1}day^{-1}$) in FMA (full lines) and JAS (dashed lines) averaged from 2015–2019 at Melax mooring location. Physical rates are shown in (a): DYN=ADV+VMIX, ADV=total advection, VMIX= vertical mixing, BIO=lumped biogeochemical rates. Biogeochemical DO rates are shown in (b): Organic matter remineralization (REMIN<0), zooplankton respiration (RESPZ<0), photosynthetic DO production by new (PNP>0) and regenerated (PRP>0) primary production. Note the different horizontal scales in (a) and (b).

5.2. Seasonal and vertical variability of the DO budget

5.2.1. Physical terms

Physical transport and mixing (DYN) remove DO in the surface layer (~0-16 m) and ventilate the water column below (Fig. 3a). The vertical mixing term (VMIX) is negative near the surface as surface oxygenated waters are mixed with the less oxygenated subsurface waters. Between 10 m depth and the bottom, vertical mixing supplies oxygen to the water column, with a maximum contribution near ~16-18 m depth (~17 $\mu molO_2L^{-1}day^{-1}$). The near-surface strongly negative (resp. positive) mixing in FMA (resp. JAS) is due to air-sea DO input (resp. output; see Fig. S13) in the model surface layer generating strong vertical gradients.

The interpretation of individual advection terms can be made difficult by the strong compensations between them (see *e.g.* the thermal balance in Gan and Allen, 2005; Chabert et al., 2023). Thus we present diagnostics that lump lateral and vertical advective contribution (ADV). ADV removes DO over the entire water column in FMA, with strongest values near 15-20 m depth (~−15 $\mu molO_2L^{-1}day^{-1}$) where the DO vertical gradient and DO vertical advection are largest (Figure not shown). ADV surface values are weak as surface flow and DO gradient are nearly perpendicular in the surface layer (Figure not shown). ADV (negative) contribution increases moderately in the BBL due to onshore bottom current penetrating marked oxygen gradients near the bottom (Fig. 4a). Positive VMIX overcompensates (negative) ADV, leading to a ventilation of the subsurface layer between ~15 m depth and the bottom. In JAS, the physical terms vary in the vertical as in FMA, changing sign near 15 m depth. However, rates are significantly weaker than in FMA, except near the bottom. Due to weaker winds, bottom currents and friction, VMIX is weaker than in FMA in the surface layer and nearly negligible between 10-25 m depth. Vertical mixing removes DO in the upper part of the BBL (~25-32 m; see Fig. 2b) and supplies DO to the bottom part. ADV is slightly negative and weak between the surface and 25 m depth. Below 25 m, it becomes positive (25-33 m) due to northward advection of oxygenated waters by the WABC (Fig. S9). In the BBL (33 m-bottom) it changes sign due to the onshore veering of the bottom current transporting offshore low oxygen waters towards the coast.

5.2.2. Biogeochemical terms

Fig. 3b displays the vertical structure of biogeochemical DO sources and sinks. In FMA, DO production by new primary production (PNP) is larger than production by regenerated primary production (PRP) in the surface layer, as the former is sustained by the wind-driven upwelling of subsurface, nitrate-replete waters north of the mooring location. Both PNP and PRP gradually decrease (due to light limitation) to approach 0 at 25 m depth. In contrast, PRP is significantly larger than PNP over the whole water column in JAS, and total DO production (PNP+PRP) is weaker (resp. slightly larger) in JAS than in FMA in the surface (resp. subsurface) layer.

Organic matter remineralization (REMIN) and zooplankton respiration (RESPZ) contribute nearly equally to oxygen consumption in the surface layer (0-15 m). At greater depths, REMIN becomes larger than RESPZ during both seasons. Note that despite a larger vertical export of particulate OM at the base of the euphotic depth in FMA, REMIN is ~50% larger in JAS than in FMA below 35 m depth. This will be investigated in more details in Section 6.2.3. RESPZ is ~20% higher in FMA than in JAS in the surface layer due to the higher phytoplankton biomass, and remains relatively high (~40% of surface value) near the bottom due to the relatively high grazing of phytoplankton and small particles by mesozooplankton, with respect to surface values.

6. Seasonal variability of the bottom DO budget over the Senegalese shelf

We now extend our analysis to the entire shelf focusing on the model bottom layer where the lowest DO concentrations are found. The model bottom layer is representative of the physical and biogeochemical mechanisms within the BBL.

6.1. Circulation and DO concentration

The seasonality of the wind forcing strongly influences bottom DO distribution over the shelf. During FMA, northerly winds (~ $0.1Nm^{-2}$, see red arrow in Fig. 4a) are upwelling-favourable. Over the innershelf

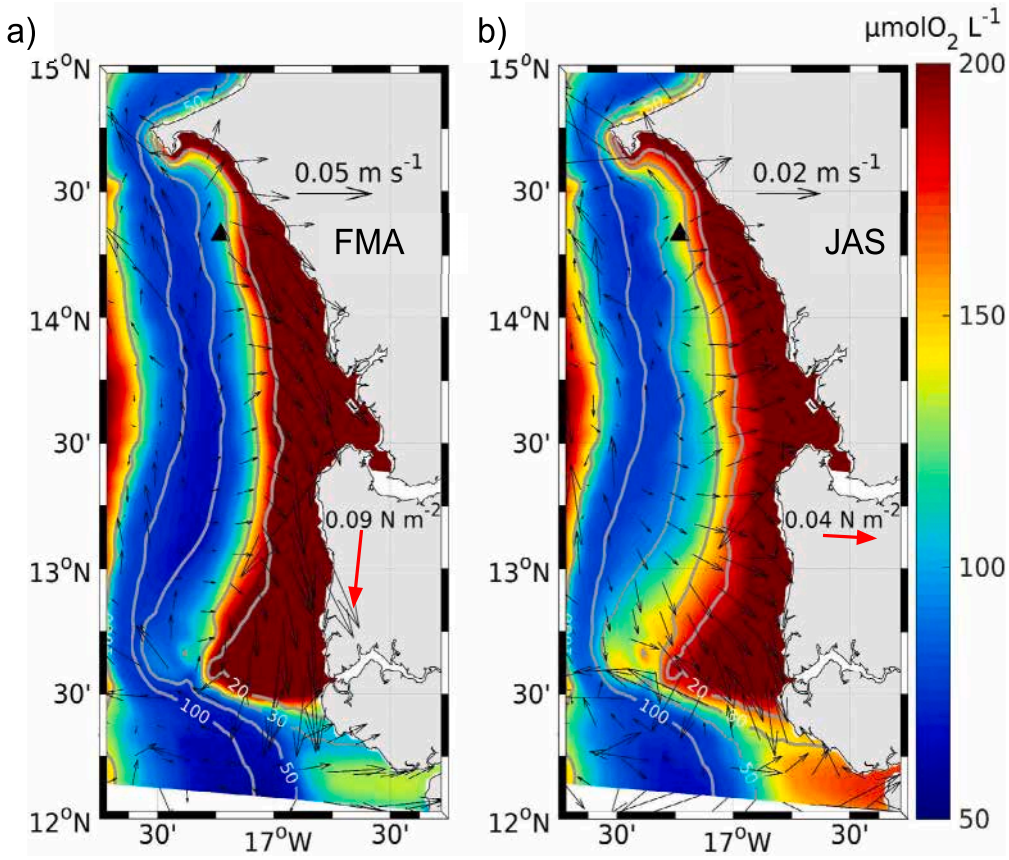

Fig. 4. Modelled bottom DO (in $\mu molO_2L^{-1}$) and bottom velocity (in cms^{-1}) in (a) FMA and (b) JAS averaged from 2015–2019. The red arrows on land represent the wind stress averaged over the shelf. The black arrows represent the bottom current (note the different vector scale in FMA and JAS). The black triangle marks the Melax location. Isobaths 20, 30, 50, 100, 1000 m depth are indicated by grey lines.

(0-20 m), bottom currents (~5-8 cms^{-1}) transport well-oxygenated bottom waters (DO> 200 $\mu molO_2L^{-1}$) south-eastward (Fig. 4a). Over the mid-shelf (20-50 m), currents are mainly directed onshore. DO cross-shore gradients are large (~80-180 $\mu molO_2L^{-1}$) over the mid-shelf (20-50 m). Over the outer shelf (*i.e.* depths greater than 50 m), the bottom current veers northward due to the influence of the WABC and DO decreases due to the proximity of the OMZ. During JAS, winds weaken (~ 0.04 Nm^{-2}) and blow eastward as the Intertropical Convergence Zone migrates northward (Fig. 4b). Bottom currents decrease (~2 cms^{-1}) and the flow over the innershelf band (0-20 m depth) is mainly onshore. Bottom waters are well oxygenated (DO> 150 $\mu molO_2L^{-1}$), more in JAS than in FMA in the 20-100 m range. The horizontal DO gradients are also much weaker in JAS than in FMA. Deeper bottom waters (h > 1000 m, near 17° 45′W) are more oxygenated (DO> 150 $\mu molO_2L^{-1}$) than over the shelf and slope as they are located below the core of the OMZ (Brandt et al., 2015).

6.2. Characterization of the DO budget

In the following, we describe the spatial patterns of the DO budget terms and their seasonal variations in the model bottom layer. Overall, consistently with results at Melax location, we find that the physical processes (DYN) supply DO to the bottom layer, while biological processes (BIO) consume DO (Fig. 5). DO supply and consumption are ~50% higher in FMA compared to JAS. Their contributions are highest (~±15 $\mu molO_2L^{-1}day^{-1}$) over the innershelf between 13° N and 14° 30′N, decrease away from the coast, and become very small at the shelf edge (h~50-100 m depth). The contributions of each physical and biogeochemical process are detailed in the following sections.

6.2.1. Physical processes

In both seasons, ventilation of the bottom layer through vertical mixing (VMIX) dominates the other terms over the shelf (Figs. 6b,h) in both seasons. VMIX intensity depends on wind stress and buoyancy forcing in the surface boundary layer (Large et al., 1994) and on bottom friction associated with the bottom currents. It is particularly intense in FMA near the coast in Hann bay south of Dakar (14° 25′N-14° 40′N), and in the ~20-30 m depth range, in particular where the bottom slope increases near 12° 30′N. High VMIX in the 20-30 m depth range corresponds to the region of enhanced DO gradient (Fig. 4a). In FMA, ADV removes DO over the shelf in a relatively narrow strip (~ $-30\ \mu molO_2L^{-1}day^{-1}$). South of 14° 20′N ADV is weaker (~ $-10-20\ \mu molO_2L^{-1}day^{-1}$). The location of the DO removal strip broadly coincides with the mid-shelf (20-30 m isobaths), where bottom currents veer onshore, nearly orthogonal to the strong cross-shore DO gradient transport (Fig. 4a). DO removal by ADV is overcompensated by ventilation by VMIX leading to a net positive contribution of the physical processes (Fig. 5a). ADV and VMIX show broadly similar patterns in JAS, but intensities are weaker and some subtle differences exist (Figs. 6g,h).

6.2.2. Biological sources and sinks

DO production is obviously confined to within the inner shelf where the euphotic layer can reach down to the bottom. In contrast with the surface layer (Fig. 3b), DO production is overcompensated by DO consumption in the bottom layer (Figs. 5b,d).

In FMA, PRP (regenerated production) is higher (~10 $\mu molO_2L^{-1}day^{-1}$) and more homogeneous over the inner shelf than PNP (new production), which is high (~5 $\mu molO_2L^{-1}day^{-1}$) mainly over the northern inner shelf downstream of the main upwelling location (13° 30′N-14°

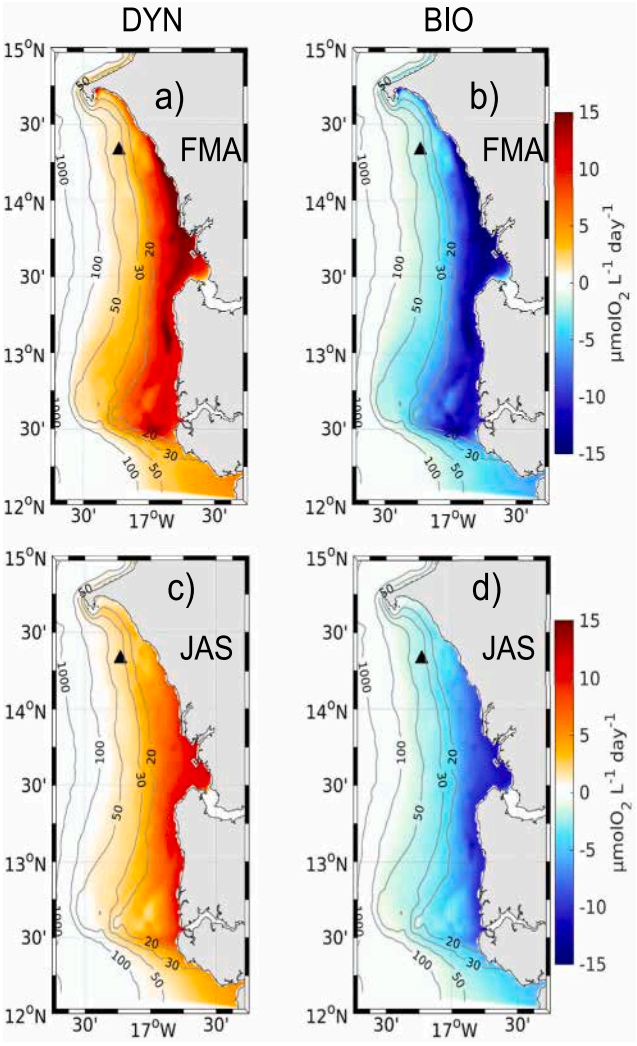

Fig. 5. Modelled DO rates (in $\mu molO_2L^{-1}day^{-1}$) in the bottom layer due to lumped (a) physical and (b) biogeochemical processes in FMA averaged from 2015–2019. (c) and (d) : same as (a) and (b) for JAS. Note that DO air-sea exchanges are not taken into account in the physical processes, as they take place in the surface layer.

45′N) and near the southern tip of the shelf (~12° 30′N). The same patterns are found in JAS albeit with lower magnitudes. The main biogeochemical DO sink is OM remineralization (REMIN, Figs. 6e,k), which dominates over zooplankton respiration (RESPZ). REMIN and RESPZ maximum rates are found over the innershelf, consistently with the higher primary production rates. REMIN rates are higher over the innershelf in FMA (~10-15 $\mu molO_2L^{-1}day^{-1}$) than in JAS (~5-10 $\mu molO_2L^{-1}day^{-1}$), likely related to the higher production rates in FMA. However, REMIN is higher in JAS over the mid shelf (20-50 m depth, Fig. 7a). Note also that a simple equilibrium exist between REMIN drawdown and VMIX ventilation over portions of the outer shelf where ADV is negligible in FMA.

6.2.3. Seasonal variability of POM export

We now explore the seasonality of the Particulate Organic Matter (POM) export to the bottom layer and its impact on DO consumption in the bottom layer (Fig. 7). POM export is defined as the downward flux of OM to the bottom layer. It is equal to the sinking velocity multiplied by the particulate OM concentration above the bottom layer for each size class. As expected from the vertical structure of primary production (Fig. 3b), export is ~50% larger in FMA than in JAS and highest near the coast (25-40 $mmolO_2m^{-2}day^{-1}$ in FMA; Fig. 7b; note that the PISCES Redfield ratio of 106/138 was used to obtain the OM oxygen content). Export in JAS reaches only 10-20 $mmolO_2m^{-2}day^{-1}$ (Fig. 7c). The remin/export ratio (hereafter REX, marked by black isolines in Figs. 7b,c) is an indicator of the amount of produced OM that is remineralized locally in the bottom layer. REX lower than 1 indicates that part of the OM exported at a certain location is transported elsewhere by bottom currents thus not remineralized locally. Predictably, low REX are systematically found in the deeper areas due to larger length of time for OM remineralization before reaching the bottom layer. However, REX is lower in FMA than in JAS everywhere, due to stronger horizontal currents (Fig. 4) and OM horizontal advection (Fig. S10). Thus, in FMA, the strong onshore currents accumulate OM over the inner shelf, enhancing remineralization there, and deplete of OM the northern mid-shelf, leading to lower remineralization rates (Fig. 7a)

7. Interannual variability of bottom DO

7.1. DO anomalies

In the following focus is given on the negative DO anomalies (relative to the DO mean seasonal cycle over 2015–2019) over the mid and outer shelf (between 20 and 100 m depth) where hypoxia occurs occasionally. Bottom DO concentration shows a strong interannual variability with DO anomalies reaching up to ~ ±40 $\mu molO_2L^{-1}$ (Fig. 8). DO anomaly patterns differ from year to year and between seasons. In FMA, the anomaly fields exhibits positive and negative patches over the shelf. Spatial scales typical for the patches tend to be larger in the alongshore direction but alternations in sign between 12° 30′N and 14° 30′N are found each year except 2016. The 2019 negative anomaly near 14° 30′N is related to an enhanced wind-driven upwelling (not shown). The largest negative anomalies are encountered over the southern part of the outer shelf (12° 45′N-13° 30′N) in 2017, leading to hypoxia. Such hypoxic waters are associated with a sluggish and weakly variable bottom circulation and longer residence time over the outer shelf, illustrated by low bottom current standard deviation (hereafter U_{std}; Table 1; Fig. S11). U_{std} is lowest in 2017 (~ $2.35 cms^{-1}$ *i.e.* 20% lower than the mean) compared to other years. DO anomalies are not related to POM export, as the highest POM export values are encountered in 2018 (Table 2).

DO anomaly fields in JAS are more homogeneous in space (Figs. 8f-j) than in FMA. Hypoxic waters are encountered in 2016 over a large portion of the shelf (13° N-14° N; 30-50 m depth). Again, bottom current standard deviation intensity in 2016 is much lower (~45%) than the mean (Table 1), suggesting a much longer residence time of bottom waters. Bottom waters are also deoxygenated in 2018 over the southern shelf and in 2019 over the northern shelf (south of Dakar), but DO levels remain above the hypoxic threshold. The high bottom current variability in JAS 2015 (Table 1) is also consistent with an anomalously high ventilation of the bottom layer (Fig. 8f).

7.2. Interannual variations of DO budget terms

As shown in Section 2.5, time-averaged DO budget terms can cause errors in the interpretation of DO anomalies averaged over a period of several months (*e.g.* FMA or JAS). In the following, we illustrate how computing the DO anomalies in FMA (or JAS) from Eq. (7) (hereafter $\Delta O_2 b$, see Fig. 9) allows to investigate the respective contribution of initial conditions and of the DO budget terms. Daily-averaged dynamical terms are used so that only an approximation of their contribution is computed using Eq. (8). We compare these anomalies with those derived straightforwardly from the model daily-averaged DO fields (hereafter $\Delta O_2 a$, see Fig. 8) by computing the relative error $\epsilon' = |(\Delta O_2 b - \Delta O_2 a)/\Delta O_2 a|$.

ϵ' for the FMA 2017 anomaly is ~25% on average over the southern mid-shelf (30-50 m, 12° 30′N-13° 30′N) where the DO anomaly is strongest (higher relative errors are found for weak anomalies, by

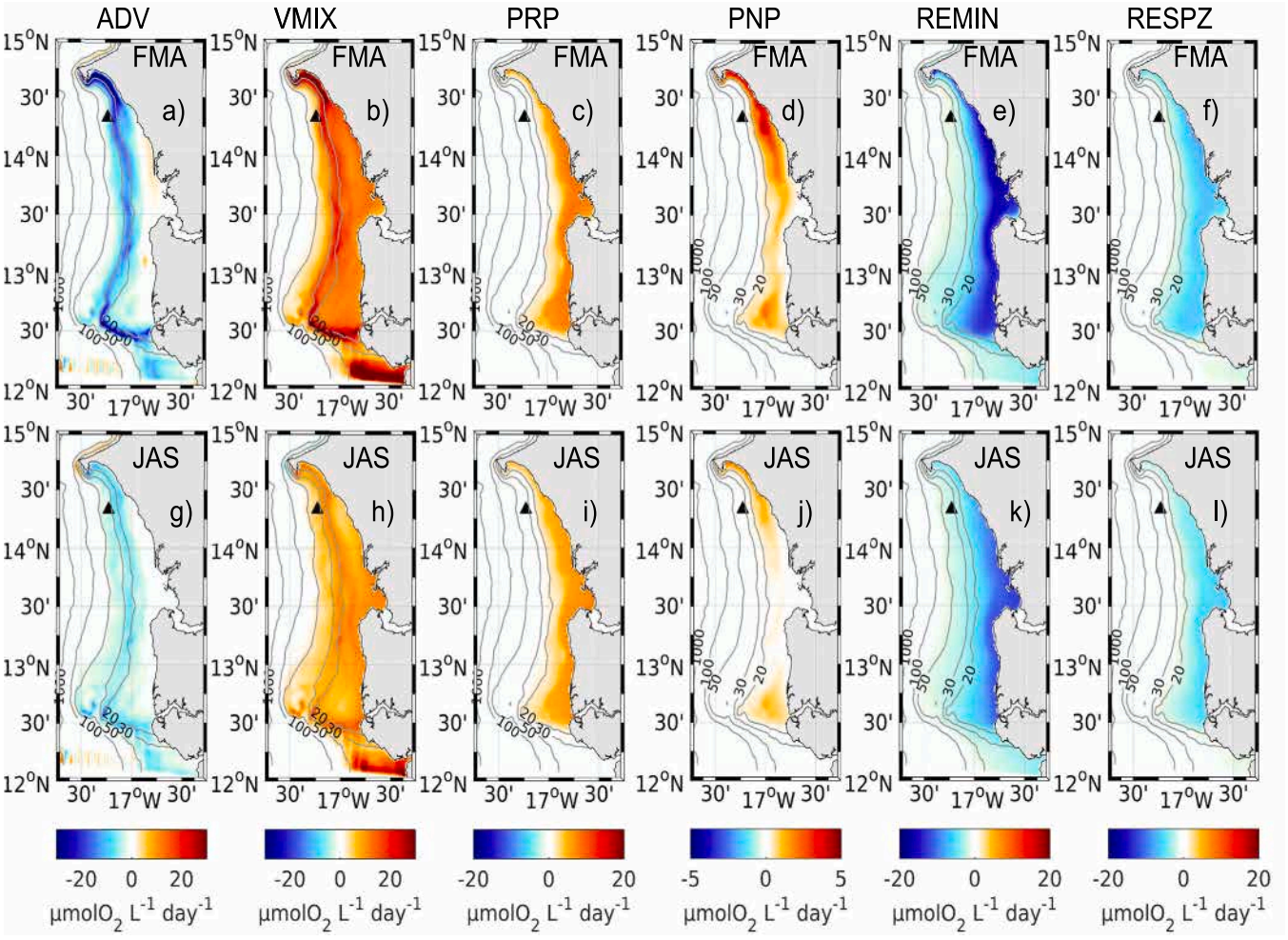

Fig. 6. Modelled DO rates (in $\mu molO_2 L^{-1} day^{-1}$) in the bottom layer due to (a) advection (ADV), (b) vertical mixing (VMIX), (c) production by regenerated primary production (PRP), (d) production by new primary production (PNP; note the different colour scale), (e) consumption by OM remineralization (REMIN), (f) zooplankton respiration (RESPZ) in FMA averaged from 2015–2019. (g–l) same as (a–f) but for JAS.

Table 1
Standard deviation of bottom velocity (30–50 m depth) in FMA (12.5 °N–13.5 °N) and JAS (13 °N–14 °N). Minimum values in JAS 2016 and FMA 2017 are highlighted in bold font. CUI is the cumulative integrated upwelling between October of year (n-1) and end of April of year (n) from ASCAT meridional wind stress at 14.8 °N, 17.5 °W.

Years	2015	2016	2017	2018	2019	*mean*
U_{std} (cms^{-1}), FMA (12.5 °N–13.5 °N)	3.61	2.97	**2.35**	2.57	3.32	2.96
U_{std} (cms^{-1}), JAS (13 °N–14 °N)	4.10	**1.72**	2.56	3.61	3.09	3.05
CUI ($Nm^{-2}day$) (14.8 °N,17.5 °W)	−6.1	−7.5	−8.4	−9.1	−9.2	−8.1

Table 2
POM carbon export (spatially averaged, in $mmolCm^{-2}day^{-1}$). The shelf is defined as the region with bottom topography less than 100 m. North shelf: 13.5 °N–14.6 °N; South shelf: 12 °N–13.5 °N.

Years	2015	2016	2017	2018	2019	*mean*
$FMA(allshelf)$	24.3	24.4	25.3	28.9	25.2	25.62
$FMA(northshelf)$	24.9	23.5	25.3	28.6	24.9	25.44
$FMA(southshelf)$	23.7	25.1	25.2	29.0	25.4	25.68
$JAS(allshelf)$	11.4	17.6	10.8	17.2	16.2	14.64

construction *e.g.* 190% in 2018). Despite this caveat, this shows that about two thirds of the FMA 2017 DO anomaly are due to the low DO concentration on February 1st, 2017 and that about one third is due to a particularly high DO biological consumption (the highest in the 2015–2019 period, not shown).

ϵ' for JAS anomalies range between 0.7% (2015) and 130% (2019), on average over the mid-shelf (30-50 m depth, 13° N-13.9° N). Concerning the hypoxic period in JAS 2016, ϵ' is very low (~3%). $\Delta O_2 b$ is fully due to the low DO on July 1st, 2016 and the integrated DO evolution during the 3 months time period is very weak (Fig. 9h). Overall, our approach based on the offline reconstruction of DO anomalies using time-averaged DO budget terms is sound and informative whenever DO anomalies are sufficiently pronounced. The results we obtained suggest that preconditioning (*i.e.* initial DO conditions) play a key role during the two hypoxic periods simulated by our model. They indicate the long persistence time scale of DO anomalies, which, once established, can

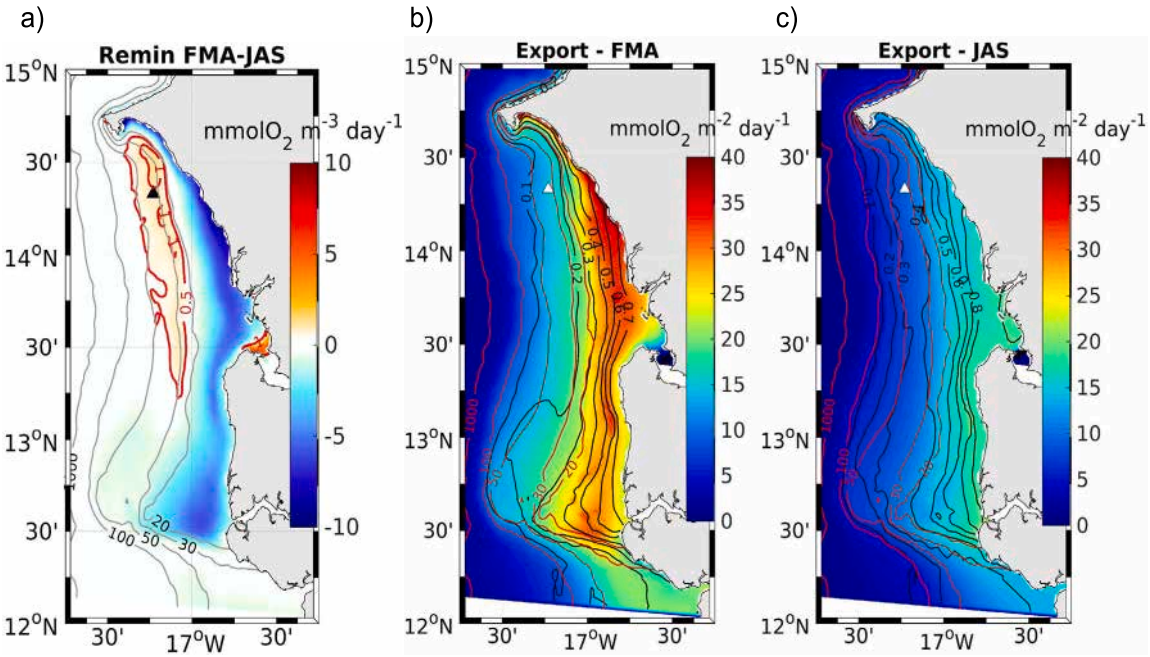

Fig. 7. (a) Remineralization difference (FMA-JAS) in the bottom layer (colour shading; in $\mu molO_2 L^{-1} day^{-1}$). Red contours show positive values where the remineralization rate in JAS is greater than in FMA. Organic oxygen export (colour shading; in $mmolO_2 m^{-2} day^{-1}$) and non-dimensional $|Remin * \Delta z|$/export ratio (REX; black contours) in (b) FMA and (c) JAS. Note that a Redfield ratio of 106/138 was used to evaluate the POM O_2 content. The 20, 30, 50, 100, 1000 m isobaths are indicated by grey lines in (a) and by red lines in (b) and (c).

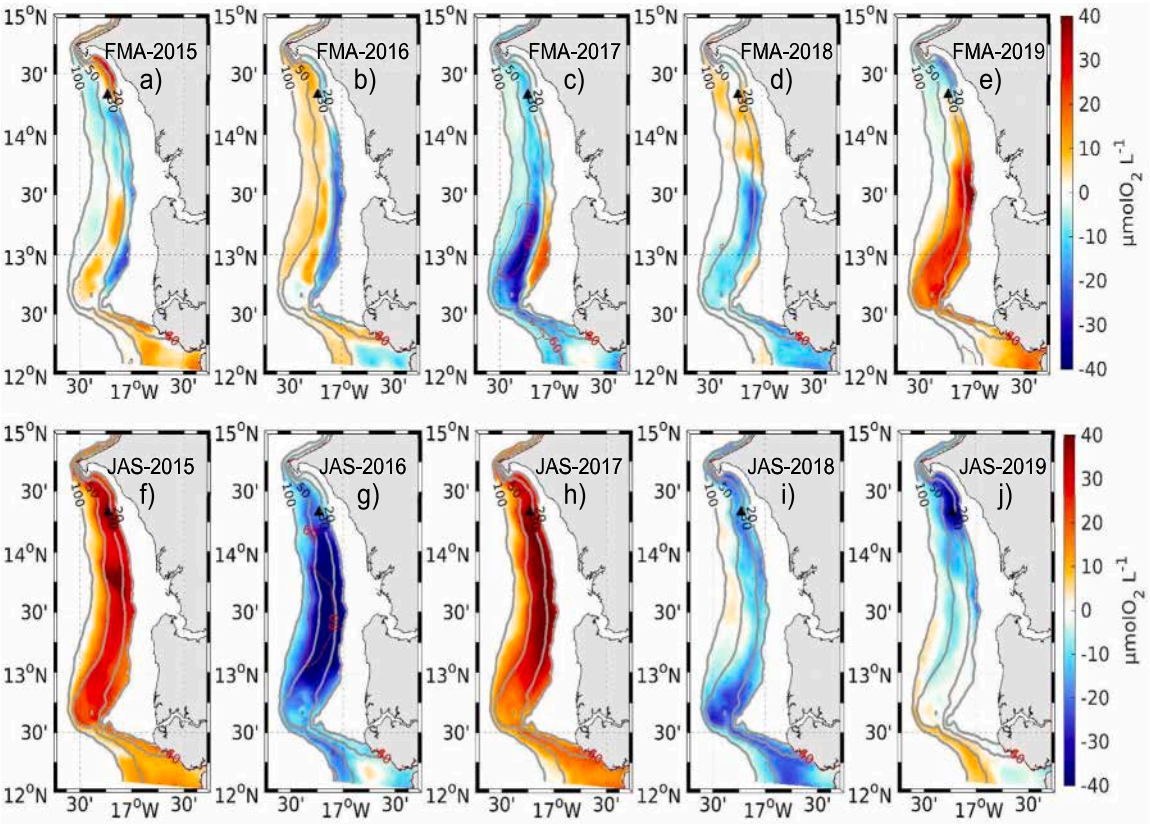

Fig. 8. DO anomalies (in $\mu molO_2 L^{-1} day^{-1}$) over the outer-shelf (20-100 m depth) in (a–e) FMA and (f–j) JAS between 2015 and 2019. Hypoxic regions are marked by the 60 $\mu molO_2 L^{-1}$ red isoline in FMA 2017 (c) and JAS 2016 (g).

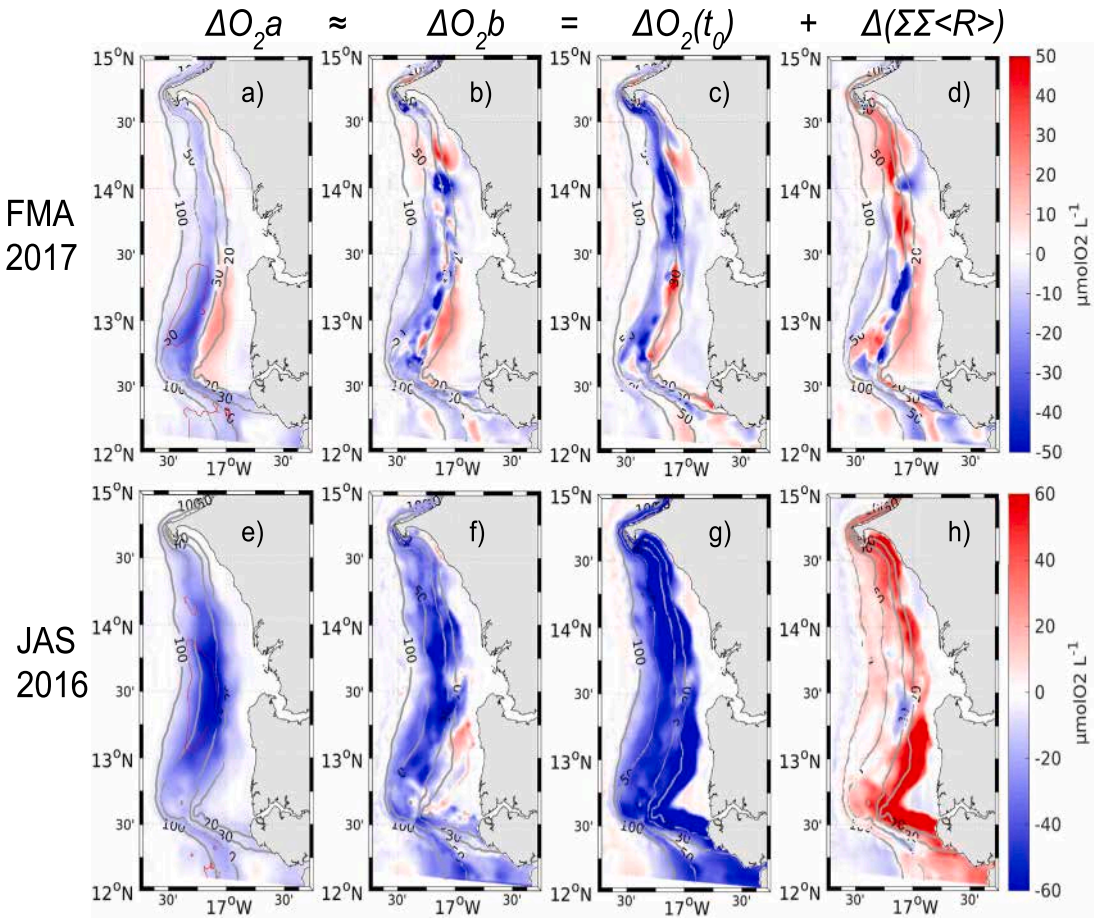

Fig. 9. Seasonal DO anomalies in FMA 2017 (a–b) and JAS 2016 (e–f) computed from daily-averaged DO model outputs ($\Delta O_2 a$:a,e) and from the sum of DO anomalous initial conditions and of the double time integrals of the DO budget terms ($\Delta O_2 b$:b,f). DO Anomalous initial conditions $\Delta O_2(t_0)$ are shown in (c,g). Anomalies of the double time integrals derived from daily-averaged DO budget terms ($\Delta(\Sigma\Sigma\langle R\rangle)$) are shown in (d,h). Hypoxic regions of the shelf are marked by the 60 $\mu molO_2L^{-1}$ red isoline in (a) and (e). Note that the same colour scale shown on the right side of each row is used for all the panels of the row, but different for FMA and JAS. Isobaths 20, 30, 50, 100 m depth are marked by grey lines.

remain over the shelf during several months (but typically not over a succession of seasons, see Fig. 8).

7.3. Lagrangian analysis

To investigate the impact of bottom water retention on DO content, Lagrangian virtual floats were released (see Section 2.6) above the sea floor (between 30 and 50 m depth) and in two different latitude bands corresponding to the hypoxic sectors found in FMA 2017 (12.8° N-13.2° N; 450 floats; Fig. 10k) and JAS 2016 (13° N-14° N; 780 floats; Fig. 11k). Floats are then tracked backward in time to characterize the pathways and DO content of the source water mass reaching the bottom layer and becoming hypoxic.

The spatial distribution of floats released in FMA shows remarkable patterns (Figs. 10a–e). The largest density of particles is located over the mid and outer shelf, above the 50-100 m isobaths. The source waters originate partly from the northern slope and SSUS shelf, but most particles reaching the bottom layers over the southern part of the shelf come from the south, following roughly the 100 m isobath. Interannual variability in the source water positions can be seen, with more particles originating from the north (resp. south) in 2016 (resp. 2015). The high density of particles found in the vicinity of the release zone in 2017 (Fig. 10c) confirms the sluggish circulation of bottom waters, which can thus be subjected to DO drawdown through remineralization. Note that POM export over the southern part of the shelf is not particularly high in 2017 (Table 2), which indicates that the anomalously slow circulation over the sea floor is the key driver of that bottom water deoxygenation episode.

The characteristics of source waters DO content are also very informative. Strong interannual variability in source water DO concentration is observed with low values in 2015 and 2017 (resp.~80 and ~75 $\mu molO_2L^{-1}$; Figs. 10f,h). The evolution of the source waters DO concentration (averaged over the floats population) during their transit towards the bottom of the shelf is quite variable depending on time and year (Fig. 10l). DO decreased on average by ~5 $\mu molO_2L^{-1}$ during the first 15 days (days −30 to −15), reaches a minimum (~80 $\mu molO_2L^{-1}$) and then increases by ~5 $\mu molO_2L^{-1}$ during the last 15 days. All years except 2019 display a deoxygenation phase varying between ~12 days (in 2015) and ~25 days (in 2017). The nearly constant deoxygenation rate (~0.75 $\mu molO_2L^{-1}day^{-1}$) during the long 2017 phase leads to hypoxia.

Lagrangian experiments in JAS show that water parcels present over the shelf bottom come from both the northern and southern part of the shelf (Fig. 11). There is little interannual variability in the spatial patterns. Source waters are strongly deoxygenated in 2016 (Fig. 11g). On average, DO increases (by ~10 $\mu molO_2L^{-1}$ in 1 month) before reaching the shelf (Fig. 11l), except in 2016 during which DO concentration decreases by ~10 $\mu molO_2L^{-1}$ during the first 25 days. Overall, DO conditions depend very much on DO values one month before. Indeed, the strong 2016 DO anomaly is mainly related to a low DO concentration (~70 $\mu molO_2L^{-1}$) at day −30 (to be compared with values between 90 and 120 $\mu molO_2L^{-1}$ in other years).

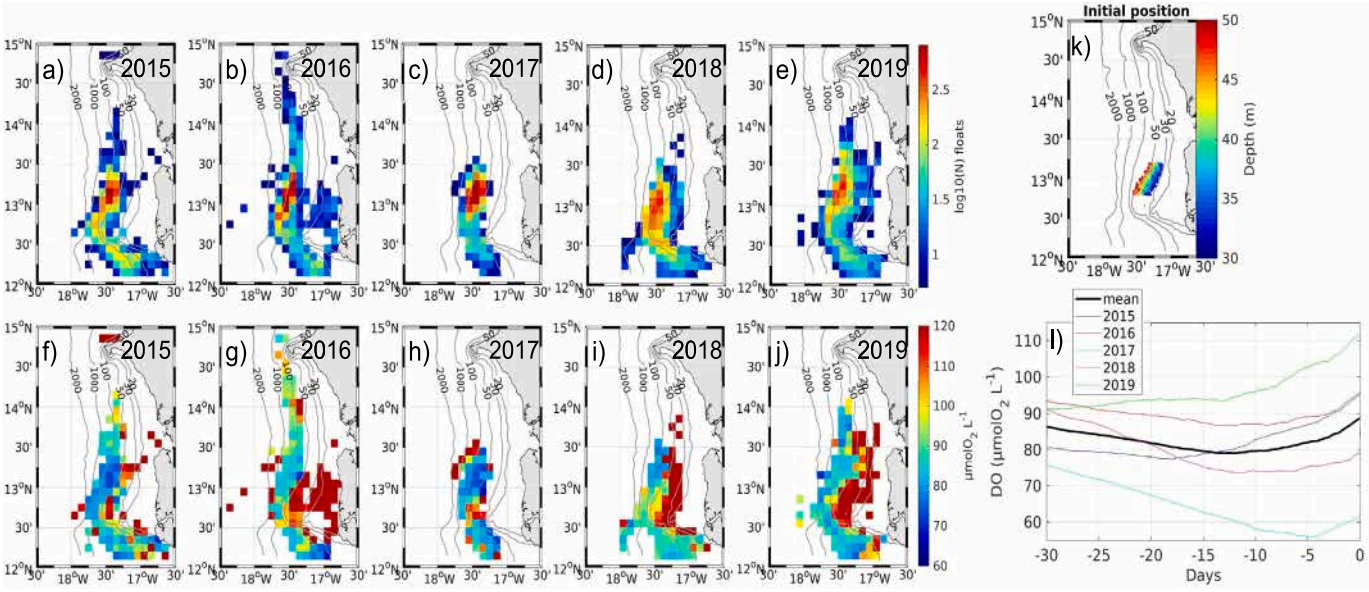

Fig. 10. (a–e) Spatial distribution of the source water particles (virtual floats) 30 days before being transported over the southern shelf (final particles positions on the shelf shown in (k) correspond to the hypoxic area in FMA 2017). Particles were binned on a regular 0.1° x0.1° grid. Pixels with less than 5 floats are not shown. (f–j) Binned source water DO concentration (in $\mu molO_2L^{-1}day^{-1}$). (l) Time evolution of the mean source water DO concentration between t = −30 days and$t = 0$ days during the cold season of each year: 2015 (blue), 2016 (red), 2017 (cyan), 2018 (magenta), and 2019 (green). The black line shows the average DO concentration of all particles.

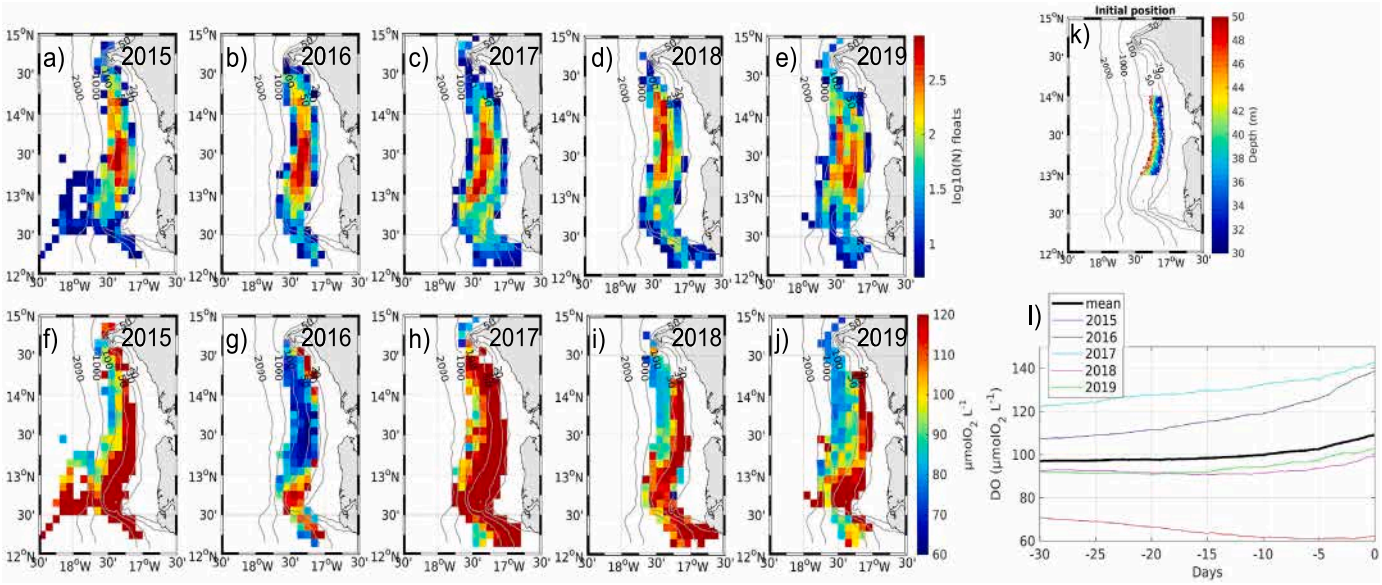

Fig. 11. Same as Fig. 9 but in JAS. In this season, floats are released between 13° N and 14° N, and between 30 and 50 m depth, which corresponds to the hypoxic area in JAS 2016.

8. DO synoptic variability

The mid-shelf (30-50 m depth) averaged DO time series in the northern (14.2° N-14.6° N) and southern (12.8° N-13.5° N) shelf show strong synoptic variability (5-15 days; Fig. S12). In this section we investigate DO evolution and mechanisms during upwelling and relaxation events. Upwelling events are defined by southward wind stress (τ_y) larger (in absolute value) than 0.04 Nm^{-2} during at least two successive days. A cumulative upwelling index (CUI=$\int \tau_y.dt$) is computed for each event. In total, 24 upwelling events are identified. Note that the analysis is extended over the entire year, not only FMA. Relaxation events (in FMA) are defined as follows: $-0.02\ Nm^{-2} \leq \tau_y \leq 0$ between two successive upwelling events.

Off the northern shelf, more than half of the upwelling events are associated with a DO decrease, except for 10 events (7 of which are associated with a weak DO increase *i.e.* less than +10 $\mu molO_2L^{-1}$; Fig. 12a). Most events have a CUI less than 1 $Nm^{-2}day$. The largest DO decrease is obtained during a strong upwelling event in 2016 (~110 $\mu molO_2L^{-1}$; CUI~2 $Nm^{-2}day$). As for the seasonal scale, typical synoptic upwelling events are characterized by DO loss due to advection and biological consumption (Figs. 12b,d) partly compensated by vertical mixing (Fig. 12c). Exceptional upwelling events (during which DO increases) are characterized by strong vertical mixing (*e.g.* ~100 $\mu molO_2L^{-1}$ in 2015) or positive advection (*e.g.* ~80 $\mu molO_2L^{-1}$ in 2016). Relatively high biological consumption occurs during these atypical events. Only 6 relaxation events are identified over the time

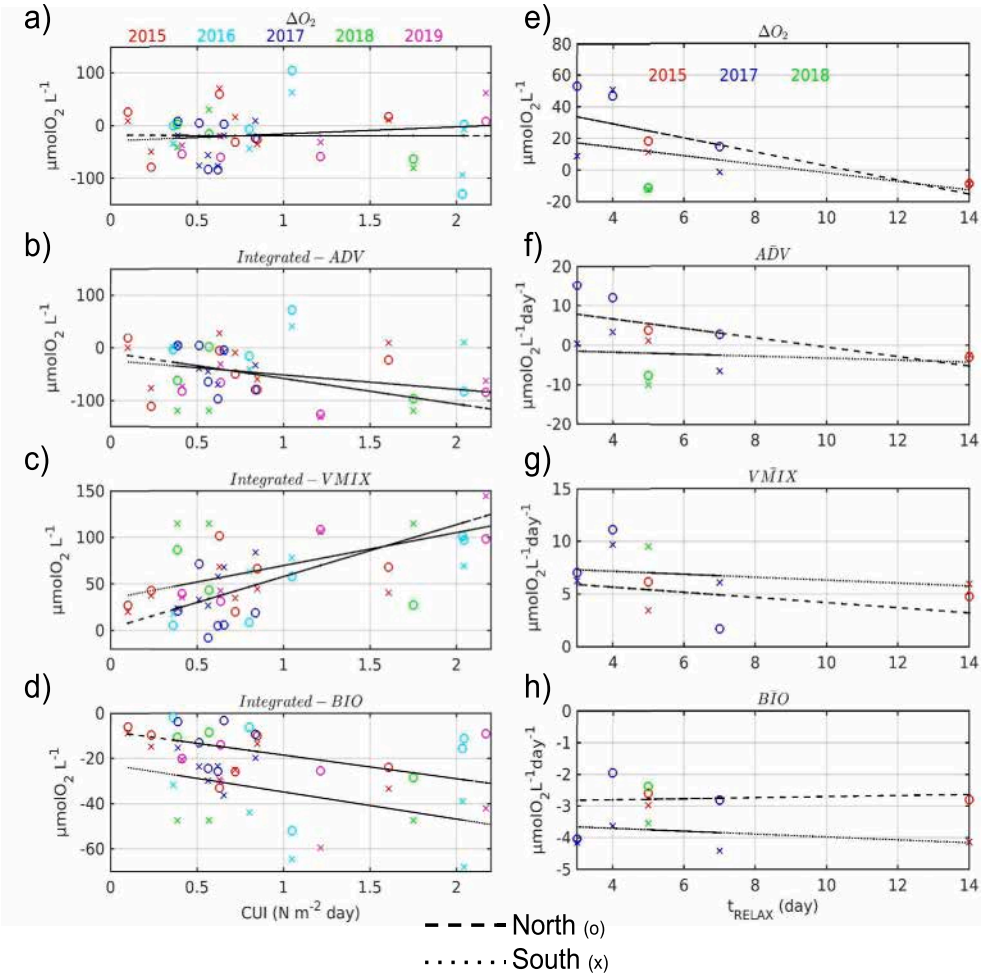

Fig. 12. (a) bottom DO change (in µmolO_2L^{-1}) with respect to CUI during upwelling events; same for time-integrated (b) advection (ADV); (c) vertical mixing (VMIX) and (d) biological (BIO) contributions. DO rates were spatially averaged over the northern (circles (o), 14.2° N-14.6° N) and southern (cross (x), 12.8° N-14.5° N) mid-shelves (30-50 m depth). FMA upwelling events are indicated by colours (2015, red; 2016, cyan; 2017, blue; 2018, green; 2019, magenta). Upwelling events are defined by the following criterion: $\tau_y \leq -0.04$ Nm^{-2} (Tall et al., 2021) for at least 2 successive days. The Cumulative Upwelling Index (CUI) is computed as CUI=$\int \tau_y.dt$. (e) Bottom DO change (in µmolO_2L^{-1}), and (f–h) average contributions of ADV, VMIX and BIO, with respect to the length (in days) of relaxation events.

period, during which DO generally increases (Fig. 12e). The longer the relaxation, the weaker the DO increase. Two events stand out with a weak DO decrease (less than 20 µmolO_2L^{-1}) driven by negative advection (in 2018) and with a strikingly long relaxation period (14 days in 2015).

Mechanisms driving synoptic DO variability are not drastically different over the southern shelf than over the northern shelf, except the larger DO biological consumption during both upwelling and relaxation events (see dotted lines in Fig. 12h). Such DO loss is likely related to the higher retention over the southern shelf than over the northern shelf (not shown) rather than to the weak differences in POM export (Table 2).

9. Discussion and conclusions

9.1. Seasonal to interannual deoxygenation over EBUS continental shelves

Intermittent hypoxia occurs over many of the continental shelves bordering EBUS, due to the proximity of deep-ocean OMZs providing source waters for coastal upwelling and to high local organic matter production. DO conditions over shelves along the eastern border of the Pacific ocean are influenced by climate oscillations such as the PDO (Pacific Decadal Oscillation) at decadal time scales (*e.g.* Duteil et al., 2018; Espinoza-Morriberón et al., 2021) and ENSO (El Nino Southern Oscillation) at interannual time scales (*e.g.* Espinoza-Morriberón et al., 2019). These large-scale oscillations induce major modifications of the coastal circulation and the generation of equatorial Kelvin waves and poleward-propagating coastal trapped waves which modulate the depth of the nearshore thermocline and oxycline. These oscillations modify the DO content of upwelling source waters, stratification and mixed layer depth, productivity and consequently OM respiration (Bograd et al., 2019).

Several studies have addressed shelf deoxygenation in the North eastern Pacific over the Oregon shelf, a region undergoing wind-driven coastal upwelling and hypoxia during summer. Seasonal hypoxia was first observed over the inner shelf (20–50 m) in 2002 (Grantham et al., 2004; Peterson et al., 2013) and then in most years (Chan et al., 2008; Barth et al., 2024). Using a regional modelling approach, Koch et al. (2017) found that late-spring preconditioning of DO and nitrate conditions over the shelf north of the deoxygenated region were key to the development of hypoxia. Although DO production due to biological processes was large, advection and vertical diffusion associated with coastal upwelling were the main drivers of hypoxia. These results are consistent with our findings, as, on average over the Senegalese shelf, bottom DO loss associated with advection is as strong as (resp. ~10% weaker than) biological consumption in FMA (resp. JAS; Table 3). However, in the bottom layer, vertical mixing is a DO source overcompensating the sink terms.

Table 3
Shelf-averaged (12 °N–15 °N, h< 100*m*) values of the DO budget terms (in $\mu molO_2L^{-1}day^{-1}$) in FMA and JAS. The DO trend equal to the sum of advection (ADV), vertical mixing (VMIX) and biogeochemical terms (BIO) is noted $\partial_t O_2$.

Years	2015		2016		2017		2018		2019		*mean*	
Seasons	*FMA*	*JAS*	*FMA*	*JAS*	*FMA*	*JAS*	*FMA*	*JAS*	*FMA*	*JAS*	*FMA*	*JAS*
ADV	−3.6	−2.3	−5.3	−2.7	−4.4	−2.3	−4.6	−3.1	−4.6	−2.8	−4.50	−2.64
VMIX	9.0	4.3	9.8	8.2	9.5	4.9	11.1	7.4	9.6	6.5	9.80	6.26
DYN	5.4	1.9	4.5	5.5	5.1	2.7	6.5	4.2	5.1	3.8	5.32	3.62
BIO	−5.2	−2.0	−4.9	−5.4	−5.4	−3.0	−6.4	−4.5	−5.2	−3.9	−5.42	−3.76
$\partial_t O_2$	0.20	−0.10	−0.43	−0.09	−0.27	−0.28	0.12	−0.28	−0.08	−0.15	−0.092	−0.144

Changes in source waters oxygen conditions also impact shelf deoxygenation (Figs. 10l, 11l). A model Lagrangian experiment similar to ours showed that source water changes in the Equatorial Pacific increased (decreased) severe hypoxia (DO< 22 $\mu molO_2L^{-1}$) during La Niña (El Niño) over the northern Peru shelf (9° S; Espinoza-Morriberón et al., 2019). The source water parcels reaching the shelf bottom were less oxygenated, originated from deeper layers and progressed slower towards the shelf during La Niña than during El Niño. Source water DO interannual variations were also larger (~50 $\mu molO_2L^{-1}$) than in our region of interest (~10-20 $\mu molO_2L^{-1}$). However the Lagrangian integrations were performed over several months in the Peru EBUS, whereas ours were limited to one month duration, constrained by the model grid southern boundary near 12° N.

In the SSUS, the impact of major climatic events on upwelling-favourable wind conditions has been investigated using atmospheric reanalyzes (Narayan et al., 2010; Pardo et al., 2011) complemented with a time series from the Dakar meteorological station (Cropper et al., 2014). The latter found a correlation of winter (DJF) North Atlantic Oscillation (NAO) with alongshore wind over the 1981–2012 period but not with SST. Correlations between upwelling-favourable winds and other indices (East Atlantic pattern, Atlantic Multidecadal Oscillation and El Niño Southern Oscillation) were not significant. Nevertheless, the implications of NAO variability on SSUS oxygen dynamics remain unknown due to lack of long-term DO monitoring and high-resolution modelling. This will be addressed in future work focusing on decadal variability and climate change.

9.2. Synoptic variability over EBUS shelves

Regarding synopticity, Koch et al. (2017) found that strong and long lasting upwelling events induced a larger DO loss over the Oregon shelf. Our results are partly consistent with this finding, as the largest DO decrease during an upwelling event (*e.g.* ΔO_2 ~−110 $\mu molO_2L^{-1}$ in 2016; Fig. 12a) over the northern shelf is associated with the largest CUI (~2 $Nm^{-2}day$). However, the relation between DO loss and CUI is not straightforward in our study as relatively high DO loss can also be obtained for upwelling events of moderate intensity (*e.g.* ~80 $\mu molO_2L^{-1}$ for a CUI of ~ 0.25 $Nm^{-2}day$ in 2015).

Using observations in the Oregon shelf, Galán et al. (2020) investigated the role of upwelling intermittence on the development of hypoxia. They found that DO depletion in summer did not follow a simple relationship with CUI as two summers with similar CUIs displayed contrasted hypoxia intensity and duration. They hypothesized that the intensity and persistence of the upwelling affected the residence time of the water masses over the shelf, thus playing a key role in the cumulative effect of biological processes leading to hypoxia. They also hypothesized that the timing, duration and the number of upwelling and relaxation events during the summer season played a key role.

These results are consistent with our findings. In our region of interest, the winters with the largest CUIs (*e.g.* FMA 2018 and 2019; see Table 1) do not undergo hypoxia. Moreover, the hypoxia encountered in FMA 2017 is associated with upwelling events with weak CUIs and with numerous relaxations (half of the total count) during which relatively high biological consumption (~3.5-4.5 $\mu molO_2L^{-1}$) takes place. The low spatial dispersion of water particles in the region of hypoxia in FMA 2017 is also related to a high residence time over the southern shelf. Likewise, hypoxia over the Oregon shelf was more intense during the season with remotely-sensed surface Chl-a values lower than the climatology (Galán et al., 2020), suggesting that surface productivity plays a secondary role. In a similar manner, POM export was slightly lower in FMA 2017 than the climatological average over the Senegalese shelf.

Overall, the link between seasonal differences among years and synoptic hypoxic events is not straightforward. In our work, we considered all wind-driven synoptic events (Fig. 12), whether they triggered hypoxia or not. As sluggish bottom currents over the shelf seem to favour seasonal hypoxia, we can hypothesize that a winter season close to the climatology with weak upwelling and relaxation synoptic events, or a summer season with weak and stable northward circulation, would favour the generation of synoptic hypoxic events. Nevertheless, a dedicated study remains to be done to clarify their relation to the seasonal conditions.

9.3. Retention over EBUS shelves

Few modelling studies have focused on retention and their impact on DO over EBUS shelves. Using a modelling approach to study summer hypoxia over the Washington and Oregon shelves, Siedlecki et al. (2015) proposed that retentive circulation processes determined the spatial patterns of seasonal hypoxia. Following a Lagrangian modelling approach similar to ours, Stone et al. (2020) studied the link between wind synopticity, productivity and retention over the central and north California shelves, but found no clear relation between wind patterns and retention times at relatively large scales (100 km), which illustrated the complexity of the synoptic response. In contrast, our Lagrangian experiments show clear evidence of sluggish circulation over the SSUS shelf during hypoxic periods. The drivers of these circulation patterns will be investigated in future studies.

9.4. Information from Earth System Model (ESM) simulations in the SSUS

The future evolution of SSUS shelf deoxygenation is related to different factors, one of the main ones being the evolution of the upwelling-favourable winds. Coupled Model Inter-comparison Project 5 (CMIP5) simulations suggest that the intensity of the Senegalo-Mauritanian winter/spring upwelling will moderately decrease in the future under the Representative Concentration Pathways 8.5 (RCP8.5) high-emission scenario, primarily because of a wind reduction linked to a northward shift of Azores anticyclone and a modulation of the low pressures over northwest Africa (Sylla et al., 2019). A more recent study based on the same regional model setting as ours confirmed this tendency but also indicated that climate-change induced stratification increase could contribute to upwelling decrease (Ndoye et al., 2025, in review). The projected coastal upwelling decrease in the future would *a priori* yield (i) a reduction of the rate at which low-oxygenated source water are being transported over the shelf by upwelling and (ii) a reduction of primary production and OM export rates into the BBL. On the other hand, ventilation via vertical mixing would also presumably decrease. Providing insight into the overall outcome will need a dedicated model approach representing these different processes.

Another critical issue lies in the ESMs coarse spatial resolution. Calil (2023) showed that a resolution as high as ~3 km (using the CROCO model) over the entire Tropical Atlantic basin was key to adequately represent the fine scale dynamics underlying the formation of eastward and westward zonal jets ventilating the Eastern Tropical North Atlantic OMZ. As such high resolution clearly unattainable in present CMIP ESM, the expected bias in the representation of the OMZ may impact DO conditions over the west African shelves.

Last, the eastward Equatorial Undercurrent (EUC), which conveys relatively oxygenated subsurface waters of equatorial origin to the SSUS by means of the Northern Equatorial Counter Current (NECC) and poleward WABC (Richardson and Reverdin, 1987; Blanke et al., 1999), is not well represented in ESMs. Based on observations, Brandt et al. (2021) found that the EUC increased and transported more equatorial waters towards the west African coastal oceans in the recent decades, possibly compensating for local climate-change induced deoxygenation. However the drivers of EUC fluctuations are not well known and recent ESM simulations have been unable to reproduce recent oxygen trends in the equatorial oceans (Stramma et al., 2012). Pending ESMs improvements and using suitable atmospheric forcing bias corrections (e.g. Ndoye et al. (2025)), downscaling climate scenarios using the current modelling setup and following the approach of Pozo Buil et al. (2023) will provide invaluable insights on the oxygen budget in the SSUS.

9.5. Modelling approach limitations

Our approach has several limitations. First, monthly climatological conditions are imposed at the open boundaries of the *can11* model domain, away from the region of interest. Examination of the MERCATOR GLOBAL-ANALYSIS-FORECAST-PHYS-001-024 biogeochemical model product (https://doi.org/10.48670/moi-00015) (which is dynamically consistent with the physical boundary conditions we used) uncovered strongly biased DO fields, thus this product was not used in our study. Dynamics local to our large model domain remains nonetheless a source of interannual variability of the source water biogeochemical properties towards the edge of the west African coastal oceans. However our model may lack sources of OMZ and nutrient interannual variability induced by perturbations of the thermohaline tropical-subtropical cells and equatorial and coastal wave guide dynamics propagating from the model western and southern open boundaries.

Secondly, river discharge during the summer–fall rainy season may impact shelf deoxygenation at regional scale: riverine nutrients may increase productivity and DO consumption, while enhanced haline-driven surface stratification may hinder ventilation by vertical mixing. While low SSS is crudely represented by SSS relaxation towards climatological observations, riverine nutrients are altogether neglected in our study due to a lack of observations. This will be the object of future work.

Thirdly, DO fluxes at the water-sediment interface due to diagenesis have not been considered in the present study, although they could play a role over the shallow inner shelf. Coupling the water column biogeochemical model with a explicit sediment model (*e.g.* Soetaert et al., 2000) or with a simplified sediment model (*e.g.* Capet et al., 2016) may be useful to investigate in more details all the processes regulating bottom DO.

Fourthly, we found that time periods preceding FMA and JAS need to be investigated in detail to better understand the interannual variability of bottom DO. Moreover, large errors (up to ~200% in the case of weak DO anomalies) are obtained for certain time periods when time-averaged (daily-averages in our case) budget terms were used for the computation of pluri-monthly DO concentrations. As outputting DO terms for every model time step is computationally unrealistic, the computation of the double time averaging of tracer budget terms during the model integration (*i.e.* online) needs to be implemented in the numerical code. Similar diagnostics have been coded in other geophysical fluid dynamics models, *e.g.* to study momentum budgets (with the Weather Research and Forecasting atmospheric model, see Oerder et al., 2016).

Last, an alternative and perhaps very informative approach to investigate the role of synoptic events on DO could be to study the impact of a single idealized wind intensification or relaxation on the Senegalese shelf oxygenation. Using a model ensemble with different initial conditions and idealized short-term (10 days) wind perturbations, Chabert et al. (2023) investigated the changes in circulation and heat budget over the shelf. The same modelling setup has been used to investigate plankton temporal and spatial variability (Chabert et al., 2024, in revision) and could be extended to DO variability in a future study.

9.6. Conclusions

We explored, using the high-resolution regional model CROCO-PISCES, physical-biogeochemical coupled ocean model, the dynamics of bottom dissolved oxygen (DO) on the southern Senegalese shelf. The focus was on understanding episodic hypoxic and anoxic events during the upwelling (February–April, FMA) and summer season (July–September, JAS). The evaluation of these simulations against recent observations have shown that the model provided a good representation of the mechanisms governing DO dynamics and variability in the Southern Senegalese Upwelling Sector (SSUC). Advection generated a higher DO loss (resp. 10% lower) than biological consumption, in the upwelling season (resp. summer), while vertical mixing was a major process against low oxygen concentration. The circulation driven by synoptic weather (upwelling intensification and relaxation phases) also affected the bottom DO concentrations on the shelf. The largest DO loss during an upwelling event was associated with the largest Cumulative Upwelling Index (CUI). However, the relationship between DO loss and CUI was not linear. Changes in source water oxygen conditions and their interannual variations also had an impact on DO decline. The hypoxic episodes experienced in FMA 2017 and JAS 2016 were mainly due to a longer residence time of the source waters, and affected by a weak ventilation rather than an excessive export of particulate organic matter. This work forms the basis for future studies of deoxygenation focusing on the impact of climate change and on the role of sediment-water exchanges over the inner shelf in anthropized coastal areas such as Hann bay south of Dakar.

CRediT authorship contribution statement

Abdoul Wahab Tall: Writing – original draft, Visualization, Methodology, Formal analysis, Data curation, Conceptualization. **Vincent Echevin:** Writing – review & editing, Writing – original draft, Supervision, Methodology, Investigation, Funding acquisition, Formal analysis, Data curation. **Xavier Capet:** Writing – review & editing, Supervision, Funding acquisition. **Eric Machu:** Writing – review & editing, Supervision, Methodology, Data curation, Conceptualization.

The authors declare that they have no known competing financial interests or personal relationships that could have appeared to influence the work reported in this paper.

Acknowledgements

A.W.Tall was funded by the IRD-ARTS program, by SOLAB ANR-18-CE32-0009, by CNRS LEFE-GMMC projects SENOX and COCASAM, and by the IRD LMI ECLAIRS2. V. Echevin and E. Machu were supported by IRD. Modelling experiments were conducted on the IDRIS HPC Jean-Zay under DARI projects A0090101140 and A0110101140. MERCATOR global ocean model outputs were provided by the E.U. Copernicus Marine Environment Monitoring Service (CMEMS).

Appendix A. Supplementary data

Supplementary material related to this article can be found online at https://doi.org/10.1016/j.dsr2.2025.105464.

Data availability

Data will be made available on request.

References

Altieri, A.H., Gedan, K.B., 2015. Climate change and dead zones. Global Change Biol. 21, 1395–1406.

Altieri, M.A., Nicholls, C.I., Henao, A., Lana, M.A., 2015. Agroecology and the design of climate change-resilient farming systems. Agron. Sustain. Dev. 35, 869–890.

Auger, P.A., Gorgues, T., Machu, E., Aumont, O., Brehmer, P., 2016. What drives the spatial variability of primary productivity and matter fluxes in the north-west african upwelling system? a modelling approach. Biogeosciences 13, 6419–6440. http://dx.doi.org/10.5194/bg-13-6419-2016, URL: https://bg.copernicus.org/articles/13/6419/2016/.

Aumont, O., Bopp, L., 2006. Globalizing results from ocean in situ iron fertilization studies. Glob. Biogeochem. Cycles 20.

Aumont, O., Éthé, C., Tagliabue, A., Bopp, L., Gehlen, M., 2015. Pisces-v2: an ocean biogeochemical model for carbon and ecosystem studies. Geosci. Model. Dev. 8, 2465–2513.

Barnier, B., Siefridt, L., Marchesiello, P., 1995. Thermal forcing for a global ocean circulation model using a three-year climatology of ecmwf analyses. J. Mar. Syst. 6, 363–380.

Barth, J., Pierce, S., Carter, B., 2024. Widespread and increasing near-bottom hypoxia in the coastal ocean off the united states pacific northwest. Sci. Rep. 14, http://dx.doi.org/10.1038/s41598-024-54476-0.

Barton, E.D., 1998. Eastern boundary of the north atlantic: northwest africa and iberia. Sea.

Beckmann, A., Haidvogel, D.B., 1993. Numerical simulation of flow around a tall isolated seamount. part i: Problem formulation and model accuracy. J. Phys. Oceanogr. 23, 1736–1753. http://dx.doi.org/10.1175/1520-0485(1993)023<1736:NSOFAA>2.0.CO;2.

Bentamy, A., Fillon, D.C., 2012. Gridded surface wind fields from metop/ascat measurements. Int. J. Remote Sens. 33, 1729–1754. http://dx.doi.org/10.1080/01431161.2011.600348.

Blanke, B., Arhan, M., Madec, G., Roche, S., 1999. Warm water paths in the equatorial atlantic as diagnosed with a general circulation model. J. Phys. Oceanogr. 29, 2753–2768. http://dx.doi.org/10.1175/1520-0485(1999)029<2753:WWPITE>2.0.CO;2.

Bograd, S.J., Schroeder, I.D., Jacox, M.G., 2019. A water mass history of the southern california current system. Geophys. Res. Lett. 46, 6690–6698.

Bopp, L., Resplandy, L., Orr, J.C., Doney, S.C., Dunne, J.P., Gehlen, M., Halloran, P., Heinze, C., Ilyina, T., Seferian, R., et al., 2013. Multiple stressors of ocean ecosystems in the 21st century: projections with cmip5 models. Biogeosciences 10, 6225–6245.

Brandt, P., Bange, H.W., Banyte, D., Dengler, M., Didwischus, S.H., Fischer, T., Greatbatch, R.J., Hahn, J., Kanzow, T., Karstensen, J., et al., 2015. On the role of circulation and mixing in the ventilation of oxygen minimum zones with a focus on the eastern tropical north atlantic. Biogeosciences 12, 489–512.

Brandt, P., Hahn, J., Schmidtko, Z., Tuschen, F., Kopte, R., Kiko, R., Bourlès, B., Czeschel, R., Dengler, et al., 2021. Atlantic equatorial undercurrent intensification counteracts warming-induced deoxygenation. Nat. Gesosci. 14, 278–282. http://dx.doi.org/10.1038/s41561-021-00716-1.

Breitburg, D., Levin, L.A., Oschlies, A., Grégoire, M., Chavez, F.P., Conley, D.J., Garçon, V., Gilbert, D., Gutiérrez, D., Isensee, K., et al., 2018. Declining oxygen in the global ocean and coastal waters. Science 359.

Calil, P.H.R., 2023. High-resolution, basin-scale simulations reveal the impact of intermediate zonal jets on the atlantic oxygen minimum zones. J. Adv. Model. Earth Syst. 15, e2022MS003158. http://dx.doi.org/10.1029/2022MS003158.

Capet, X., Estrade, P., Machu, E., Ndoye, S., Grelet, J., Lazar, A., Marié, L., Dausse, D., Brehmer, P., 2017. On the dynamics of the southern senegal upwelling center: observed variability from synoptic to superinertial scales. J. Phys. Oceanogr. 47, 155–180.

Capet, A., Meysman, F.J., Akoumianaki, I., Soetaert, K., Grégoire, M., 2016. Integrating sediment biogeochemistry into 3d oceanic models: A study of benthic-pelagic coupling in the black sea. Ocean. Model. 101, 83–100. http://dx.doi.org/10.1016/j.ocemod.2016.03.006.

Carr, S.D., Capet, X.J., McWilliams, J.C., Pennington, J.T., Chavez, F.P., 2008. The influence of diel vertical migration on zooplankton transport and recruitment in an upwelling region: Estimates from a coupled behavioral-physical model. Fisheries Oceanography 17, 1–15.

Caverivière, A., Touré, D., 1990. Note sur les mortalités de mérou (serranidae) observées en fin de saison chaude devant les côtes du Sénégal, particulièrement en 1987. Document Scientifique - CRODT, CRODT, Dakar Thiaroye. URL: https://www.documentation.ird.fr/hor/fdi:34044.

Chabert, P., Capet, X., Echevin, V., Lazar, A., Hourdin, C., Ndoye, S., 2023. Impact of synoptic wind intensification and relaxation on the dynamics and heat budget of the south senegalese upwelling sector. J. Phys. Oceanogr. 53, 1041–1067.

Chabert, P., Echevin, V., Aumont, O., Person, R., Hourdin, C., Pous, S., Machu, E., Capet, X., 2024. Bottom-up propagation of synoptic wind intensification and relaxation in the planktonic ecosystem of the south senegalese upwelling sector. J. Plankton Res. 1–14. http://dx.doi.org/10.1093/plankt/fbae054.

Chan, F., Barth, J., Lubchenco, J., Kirincich, A., Weeks, H., Peterson, W.T., Menge, B., 2008. Emergence of anoxia in the california current large marine ecosystem. Science 319, 920.

Cheung, W.W., Sarmiento, J.L., Dunne, J., Frölicher, T.L., Lam, V.W., Palomares, M.D., Watson, R., Pauly, D., 2013. Shrinking of fishes exacerbates impacts of global ocean changes on marine ecosystems. Nat. Clim. Chang. 3, 254–258.

Correa, K., Machu, E., Brajard, J., Diouf, D., Sall, S.M., Demarcq, H., 2023. Adaptation of a neuro-variational algorithm from seawifs to modis-aqua sensor for the determination of atmospheric and oceanic variables. Remote. Sens. 15, http://dx.doi.org/10.3390/rs15143613, URL: https://www.mdpi.com/2072-4292/15/14/3613.

Cropper, T.E., Hanna, E., Bigg, G.R., 2014. Spatial and temporal seasonal trends in coastal upwelling off northwest africa, 1981–2012. Deep. Sea Res. Part I: Ocean. Res. Pap. 86, 94–111. http://dx.doi.org/10.1016/j.dsr.2014.01.007, URL: https://www.sciencedirect.com/science/article/pii/S0967063714000181.

Debreu, L., Marchesiello, P., Penven, P., Cambon, G., 2012. Two-way nesting in split-explicit ocean models: Algorithms, implementation and validation. Ocean. Model. 49, 1–21.

Duteil, O., Oschlies, A., Böning, C.W., 2018. Pacific decadal oscillation and recent oxygen decline in the eastern tropical pacific ocean. Biogeosciences 15, 7111–7126. http://dx.doi.org/10.5194/bg-15-7111-2018, URL: https://bg.copernicus.org/articles/15/7111/2018/.

Espinoza-Morriberón, D., Echevin, V., Colas, F., Tam, J., Gutierrez, D., Graco, M., Ledesma, J., Quispe-Ccalluari, C., 2019. Oxygen variability during enso in the tropical south eastern pacific. Front. Mar. Sci. 5 (526).

Espinoza-Morriberón, D., Echevin, V., Gutiérrez, D., Tam, J., Graco, M., Ledesma, J., Colas, F., 2021. Evidences and drivers of ocean deoxygenation off peru over recent past decades. Sci. Rep. 11, 1–10.

Ferry, N., Parent, L., Garric, G., Barnier, B., Jourdain, N.C., et al., 2010. Mercator global eddy permitting ocean reanalysis glorys1v1: Description and results. Mercator-Ocean. Q. Newsl. 36, 15–27.

Galán, A., Zirbel, M.J., Saldías, G.S., Chan, F., Letelier, R., 2020. The role of upwelling intermittence in the development of hypoxia and nitrogen loss over the oregon shelf. J. Mar. Syst. 207, 103342. http://dx.doi.org/10.1016/j.jmarsys.2020.103342.

Gan, J., Allen, J.S., 2005. Modeling upwelling circulation off the oregon coast. J. Geophys. Res.: Ocean. 110, http://dx.doi.org/10.1029/2004JC002692, URL: https://agupubs.onlinelibrary.wiley.com/doi/abs/10.1029/2004JC002692, arXiv:https://agupubs.onlinelibrary.wiley.com/doi/pdf/10.1029/2004JC002692.

Garcia, HE, Weathers, KW, Paver, CR, Smolyar, I, Boyer, TP, Locarnini, MM, Zweng, MM, Mishonov, AV, Baranova, OK, Seidov, D, Reagan, Jr, 2019. World Ocean Atlas 2018, Volume 3: Dissolved Oxygen, Apparent Oxygen Utilization, and Dissolved Oxygen Saturation.

Gilbert, D., Rabalais, N., Diaz, R., Zhang, J., 2010. Evidence for greater oxygen decline rates in the coastal ocean than in the open ocean. Biogeosciences 7, 2283–2296.

Glessmer, M.S., Eden, C., Oschlies, A., 2009. Contribution of oxygen minimum zone waters to the coastal upwelling off mauritania. Prog. Oceanogr. 83, 143–150.

Grantham, B.A., Chan, F., Nielsen, K.J., Fox, D.S., Barth, J.A., Huyer, A., Lubchenco, J., Menge, B.A., 2004. Upwelling-driven nearshore hypoxia signals ecosystem and oceanographic changes in the northeast pacific. Nature 429, 749–754.

Hilt, M., Auclair, F., Benshila, R., Bordois, L., Capet, X., Debreu, L., Dumas, F., Jullien, S., Lemarié, F., Marchesiello, P., Nguyen, C., Roblou, L., 2020. Numerical modelling of hydraulic control, solitary waves and primary instabilities in the strait of gibraltar. Ocean. Model. 151, 101642. http://dx.doi.org/10.1016/j.ocemod.2020.101642.

Keeling, R.F., Körtzinger, A., Gruber, N., 2010. Ocean deoxygenation in a warming world. Annu. Rev. Mar. Sci. 2, 199–229.

Key, R.M., Kozyr, A., Sabine, C.L., Lee, K., Wanninkhof, R., Bullister, J.L., Feely, R.A., Millero, F.J., Mordy, C., Peng, T.H., 2004. A global ocean carbon climatology: Results from global data analysis project (glodap). Glob. Biogeochem. Cycles 18.

Koch, A.O., Spitz, Y.H., Batchelder, H.P., 2017. Oregon shelf hypoxia modeling. In: Modeling Coastal Hypoxia: Numerical Simulations of Patterns, Controls and Effects of Dissolved Oxygen Dynamics. pp. 215–238.

Körtzinger, A., Koeve, W., Kähler, P., Mintrop, L., 2001. C: N ratios in the mixed layer during the productive season in the northeast atlantic ocean. Deep. Sea Res. Part I: Ocean. Res. Pap. 48, 661–688.

Kounta, L., Capet, X., Jouanno, J., Kolodziejczyk, N., Sow, B., Gaye, A.T., 2018. A model perspective on the dynamics of the shadow zone of the eastern tropical north atlantic–part 1: the poleward slope currents along west africa. Ocean. Sci. 14, 971–997.

Kwiatkowski, L., Torres, O., Bopp, L., Aumont, O., Chamberlain, M., Christian, J.R., Dunne, J.P., Gehlen, M., Ilyina, T., John, J.G., et al., 2020. Twenty-first century ocean warming, acidification, deoxygenation, and upper-ocean nutrient and primary production decline from cmip6 model projections. Biogeosciences 17, 3439–3470.

Large, W.G., McWilliams, J.C., Doney, S.C., 1994. Oceanic vertical mixing: A review and a model with a nonlocal boundary layer parameterization. Rev. Geophys. 32, 363–403.

Long, M.C., Deutsch, C., Ito, T., 2016. Finding forced trends in oceanic oxygen. Glob. Biogeochem. Cycles 30, 381–397.

Machu, É., Capet, X., Estrade, P., Ndoye, S., Brajard, J., Baurand, F., Auger, P.A., Lazar, A., Brehmer, P., 2019. First evidence of anoxia and nitrogen loss in the southern canary upwelling system. Geophys. Res. Lett. 46, 2619–2627.

Narayan, N., Paul, A., Mulitza, S., Schulz, M., 2010. Trends in coastal upwelling intensity during the late 20th century. Ocean. Sci. 6, 815–823. http://dx.doi.org/10.5194/os-6-815-2010, URL: https://os.copernicus.org/articles/6/815/2010/.

Ndoye, S., 2016. Fonctionnement dynamique du centre d'upwelling sud-sénégalais: approche par la modélisation réaliste et l'analyse d'observations satellite de température de surface de la mer (Ph.D. thesis). Université Pierre et Marie Curie-Paris VI; Université Cheikh Anta Diop (Dakar.

Ndoye, S., Capet, X., Estrade, P., Sow, B., Dagorne, D., Lazar, A., Gaye, A., Brehmer, P., 2014. Sst patterns and dynamics of the southern senegal-gambia upwelling center. J. Geophys. Res.: Ocean. 119, 8315–8335.

Ndoye, S., Capet, X., Estrade, P., Sow, B., Machu, E., Brochier, T., Döring, J., Brehmer, P., 2017. Dynamics of a low-enrichment high-retention upwelling center over the southern senegal shelf. Geophys. Res. Lett. 44, 5034–5043.

Ndoye, S, Echevin, V, Mignot, J, Capet, X, 2025. Impact of climate change on the dynamics of the southern senegal upwelling center. Geophysical Research Letters 52 (2), e2024GL112582.

Oerder, V., Colas, F., Echevin, V., Masson, S., Hourdin, C., Jullien, S., Madec, G., Lemarié, F., 2016. Mesoscale sst–wind stress coupling in the peru–chile current system: Which mechanisms drive its seasonal variability? Clim. Dyn. 47, 2309–2330.

Oschlies, A., Brandt, P., Stramma, L., Schmidtko, S., 2018. Drivers and mechanisms of ocean deoxygenation. Nat. Geosci. 11, 467–473.

Pardo, P., Padín, X., Gilcoto, M., Farina-Busto, L., Pérez, F., 2011. Evolution of upwelling systems coupled to the long-term variability in sea surface temperature and ekman transpor. Clim. Res. 48, 231–246.

Peterson, J.O., Morgan, C.A., Peterson, W.T., Lorenzo, E.D., 2013. Seasonal and interannual variation in the extent of hypoxia in the northern california current from 1998–2012. Limnol. Oceanogr. 58, 2279–2292.

Pitcher, G.C., Aguirre-Velarde, A., Breitburg, D., Cardich, J., Carstensen, J., Conley, D.J., Dewitte, B., Engel, A., Espinoza-Morriberón, D., Flores, G., et al., 2021. System controls of coastal and open ocean oxygen depletion. Prog. Oceanogr. 197, 102613.

Pozo Buil, M., Fiechter, J., Jacox, M.G., Bograd, S.J., Alexander, M.A., 2023. Evaluation of different bias correction methods for dynamical downscaled future projections of the california current upwelling system. Earth Space Sci. 10 (e2023EA003121), http://dx.doi.org/10.1029/2023EA003121, URL: https://agupubs.onlinelibrary.wiley.com/doi/abs/10.1029/2023EA003121, arXiv:https://agupubs.onlinelibrary.wiley.com/doi/pdf/10.1029/2023EA003121. e2023EA003121 2023EA003121.

Rabalais, N.N., Cai, W.J., Carstensen, J., Conley, D.J., Fry, B., Hu, X., Quinones-Rivera, Z., Rosenberg, R., Slomp, C.P., Turner, R.E., et al., 2014. Eutrophication-driven deoxygenation in the coastal ocean. Oceanography 27, 172–183.

Redfield, A., Ketchum, B., Richards, F., et al., 1963. The influence of organisms on the composition of seawater. Sea 2, 26–77.

Richardson, P.L., Reverdin, G., 1987. Seasonal cycle of velocity in the atlantic north equatorial countercurrent as measured by surface drifters, current meters, and ship drifts. J. Geophys. Res.: Ocean. 92, 3691–3708. http://dx.doi.org/10.1029/JC092iC04p03691, URL: https://agupubs.onlinelibrary.wiley.com/doi/abs/10.1029/JC092iC04p03691, arXiv:https://agupubs.onlinelibrary.wiley.com/doi/pdf/10.1029/JC092iC04p03691.

Risien, C.M., Chelton, D.B., 2008. A global climatology of surface wind and wind stress fields from eight years of quikscat scatterometer data. J. Phys. Oceanogr. 38, 2379–2413.

Rose, K.A., Gutiérrez, D., Breitburg, D., Conley, D., Craig, K.J., Froehlich, H.E., Jeyabaskaran, R., Kripa, V., Mbaye, B.C., Mohamed, K., Padua, S., Prema, D., 2019. Impacts of ocean deoxygenation on fisheries. In: Ocean Deoxygenation: Everyone's Problem. Causes, Impacts, Consequences and Solutions. International Union for Conservation of Nature and Natural Resources, pp. 519–544.

Roy, C., 1989. Fluctuations des vents et variabilité de l'upwelling devant les côtes de sénégal. Oceanol. Acta 12, 361–369.

Sathyendranath, S., Brewin, R., Brockmann, C., Brotas, V., Calton, B., Chuprin, A., Cipollini, P., Couto, A., Dingle, J., Doerffer, R., Donlon, C., Dowell, M., Farman, A., Grant, M., Groom, S., Horseman, A., Jackson, T., Krasemann, H., Lavender, S., Martinez-Vicente, V., Mazeran, C., Mélin, F., Moore, T., Müller, D., Regner, P., Roy, S., Steele, C., Steinmetz, F., Swinton, J., Taberner, M., Thompson, A., Valente, A., Zühlke, M., Brando, V., Feng, H., Feldman, G., Franz, B., Frouin, R., Gould, R., Hooker, S., Kahru, M., Kratzer, S., Mitchell, B., Muller-Karger, F., Sosik, H., Voss, K., Werdell, J., Platt, T., 2019. An ocean-colour time series for use in climate studies: The experience of the ocean-colour climate change initiative (oc-cci). Sensors 19 (4285), http://dx.doi.org/10.3390/s19194285.

Schmidt, M., Eggert, A., 2016. Oxygen cycling in the northern benguela upwelling system: Modelling oxygen sources and sinks. Prog. Oceanogr. 149, 145–173.

Schmidtko, S., Stramma, L., Visbeck, M., 2017. Decline in global oceanic oxygen content during the past five decades. Nature 542, 335–339.

Siedlecki, S.A., Banas, N.S., Davis, K.A., Giddings, S., Hickey, B.M., MacCready, P., Connolly, T., Geier, S., 2015. Seasonal and interannual oxygen variability on the washington and oregon continental shelves. J. Geophys. Res.: Ocean. 120, 608–633.

Soetaert, K., Middelburg, J.J., Herman, P.M., Buis, K., 2000. On the coupling of benthic and pelagic biogeochemical models. Earth-Sci. Rev. 51, 173–201.

Stone, H.B., Banas, N.S., MacCready, P., Kudela, R.M., Ovall, B., 2020. Linking chlorophyll concentration and wind patterns using satellite data in the central and northern california current system. Front. Mar. Sci. 7, http://dx.doi.org/10.3389/fmars.2020.551562, URL: https://www.frontiersin.org/articles/10.3389/fmars.2020.551562.

Stramma, L., Oschlies, A., Schmidtko, S., 2012. Mismatch between observed and modeled trends in dissolved upper-ocean oxygen over the last 50 yr. Biogeosciences 9, 4045–4057. http://dx.doi.org/10.5194/bg-9-4045-2012, URL: https://bg.copernicus.org/articles/9/4045/2012/.

Sylla, A., Mignot, J., Capet, X., Gaye, A.T., 2019. Weakening of the senegalo–mauritanian upwelling system under climate change. Clim. Dyn. 53, 4447–4473.

Takahashi, T., Broecker, W.S., Langer, S., 1985. Redfield ratio based on chemical data from isopycnal surfaces. J. Geophys. Res.: Ocean. 90, 6907–6924.

Tall, A.W., Machu, E., Echevin, V., Capet, X., Pietri, A., Corréa, K., Sall, S.M., Lazar, A., 2021. Variability of dissolved oxygen in the bottom layer of the southern senegalese shelf. J. Geophys. Res.: Ocean. e2020JC016854.

Tegen, I., Fung, I., 1994. Modeling of mineral dust in the atmosphere: Sources, transport, and optical thickness. J. Geophys. Res.: Atmos. 99, 22897–22914.

Thomsen, S., Karstensen, J., Kiko, R., Krahmann, G., Dengler, M., Engel, A., 2019. Remote and local drivers of oxygen and nitrate variability in the shallow oxygen minimum zone off mauritania in june 2014. Biogeosciences 16, 979–998.

Worley, S.J., Woodruff, S.D., Reynolds, R.W., Lubker, S.J., Lott, N., 2005. Icoads release 2.1 data and products. Int. J. Climatol.: A J. R. Meteorol. Soc. 25, 823–842.